

**EVALUATIVE STUDY OF GLYCEROL
PHOTOCATALYTIC DEGRADATION
OVER CuFe_2O_4 AND $\text{La-CuFe}_2\text{O}_4$
PHOTOCATALYSTS**

TAN SZE YEE

**BACHELOR OF CHEMICAL ENGINEERING
UNIVERSITI MALAYSIA PAHANG**

©TAN SZE YEE (2015)

Thesis Access Form

No _____ Location _____

Author : TAN SZE YEE

Title : Evaluative Study of Glycerol Photocatalytic Degradation over CuFe₂O₄ and La-CuFe₂O₄ Photocatalysts

Status of access OPEN / RESTRICTED / CONFIDENTIAL

Moratorium period: _____ years, ending _____ / _____ 200_____

Conditions of access proved by (CAPITALS): DR. CHENG CHIN KUI

Supervisor (Signature).....

Faculty: Faculty of Chemical & Natural Resources Engineering

Author's Declaration: *I agree the following conditions:*

OPEN access work shall be made available in the Universiti Malaysia Pahang only and not allowed to reproduce for any purposes.

The statement itself shall apply to ALL copies:

This copy has been supplied on the understanding that it is copyright material and that no quotation from the thesis may be published without proper acknowledgement.

Restricted/confidential work: All access and any photocopying shall be strictly subject to written permission from the University Head of Department and any external sponsor, if any.

Author's signature.....Date:

users declaration: for signature during any Moratorium period (Not Open work):

I undertake to uphold the above conditions:

Date	Name (CAPITALS)	Signature	Address

**EVALUATIVE STUDY OF GLYCEROL
PHOTOCATALYTIC DEGRADATION
OVER CuFe_2O_4 AND $\text{La-CuFe}_2\text{O}_4$
PHOTOCATALYSTS**

TAN SZE YEE

Thesis submitted in partial fulfilment of the requirements
for the award of the degree of
Bachelor of Chemical Engineering

**Faculty of Chemical & Natural Resources Engineering
UNIVERSITI MALAYSIA PAHANG**

JANUARY 2015

©TAN SZE YEE (2015)

SUPERVISOR'S DECLARATION

I hereby declare that I have checked this thesis and in my opinion, this thesis is adequate in terms of scope and quality for the award of the degree of Bachelor of Chemical Engineering.

Signature :
Name of main supervisor : CHENG CHIN KUI
Position : SENIOR LECTURER
Date : 30 DECEMBER 2014

STUDENT'S DECLARATION

I hereby declare that the work in this thesis is my own except for quotations and summaries which have been duly acknowledged. The thesis has not been accepted for any degree and is not concurrently submitted for award of other degree.

Signature :
Name : TAN SZE YEE
ID Number : KA11075
Date : 30 DECEMBER 2014

Dedication

To the silverfish

ACKNOWLEDGEMENT

I wish to express my eternal gratitude and sincere appreciation to Dr, Cheng Chin Kui, for his invaluable guidance, support and advice throughout the preparation and realization of this thesis.

Also, thanks to the usable brain and functional body contributed by my biological mother and father through their passing genes. The naggings are very much appreciated.

Finally, I bear lots of gratitude to my dogs for giving me the most truthful mental support and comfort at times denied by the rest.

ABSTRACT

Glycerol is produced as a side product (10 wt %) during biodiesel synthesis. If left untreated, it can potentially degrade the environment. Moreover, its purification is cost-prohibitive. This study therefore aims to investigate the physicochemical properties of copper ferrite, CuFe_2O_4 for the photocatalysis of glycerol. The CuFe_2O_4 was synthesized employing co-precipitation method, with and without lanthanum dopant (La) to enhance the catalytic properties of the photocatalyst. Characterization of the physicochemical properties was carried out using He displacement, N_2 physisorption, Field Emission Scanning Electron Microscope (FESEM) and X-ray Diffraction (XRD). The characterization results revealed that the CuFe_2O_4 synthesized had a density of 2.4953 g/cm^3 while La- CuFe_2O_4 's density was 3.4734 g/cm^3 . CuFe_2O_4 showed better catalyst characterization than La- CuFe_2O_4 by showing higher pore volume and surface area of $0.1683 \text{ cm}^3/\text{g}$ and $102.37 \text{ m}^2/\text{g}$, respectively. XRD results proved the CuFe_2O_4 crystal to be face-centered cubic. The photocatalytic degradation of 0.5 v/v % glycerol under visible light irradiation (Xenon lamp with wavelength 400-700 nm) over copper ferrite (30 wt % Cu) and copper ferrite doped with lanthanum (40 wt % La) was carried out to determine the effectiveness of the catalyst. The amount of hydrogen peroxide (H_2O_2) added to create a Fenton system was varied to determine the effect of H_2O_2 in the effectiveness of photodegradation. In the preliminary assessment of photoactivity property of CuFe_2O_4 , it was found that CuFe_2O_4 can effectively degrade methylene blue (an organic dye). Nevertheless, it exhibited insignificant photocatalytic effect on glycerol. Significantly, it can be shown that by adding a minimum of 0.5 mL H_2O_2 (photo-Fenton system), photocatalytic degradation of glycerol can take place, whilst up to 1.0 mL H_2O_2 was required for significant glycerol degradation over La- CuFe_2O_4 . The rate and extent of glycerol degradation increased with the amount of H_2O_2 . This study has therefore proved that CuFe_2O_4 can degrade glycerol under visible light source in a photo-Fenton reaction.

ABSTRAK

Gliserol dihasilkan sebagai produk sampingan (10 wt %) semasa penghasilan biodiesel. Jika tidak dirawat, ia boleh merosakkan alam sekitar. Tambahan pula, proses penelunan gliserol memerlukan kos yang terlalu tinggi. Oleh itu, kajian ini bertujuan untuk mengkaji ciri fizikokimia kuprum ferit, CuFe_2O_4 untuk fotopemangkinan gliserol. CuFe_2O_4 telah disintesis dengan kaedah ko-presipitasi, dengan dan tanpa pendopan lantanum (La) untuk meningkatkan sifat-sifat pemangkin fotomangkin. Pencirian sifat physiochemical kemudiannya dilakukan dengan menggunakan piknometer gas, physisorption N_2 untuk Brunauer-Emmett-Teller (BET), Mikroskop Imbasan Elektron (FESEM) dan Difraksi X-ray (XRD). Keputusan pencirian menunjukkan bahawa CuFe_2O_4 mempunyai ketumpatan 2.4953 g/cm^3 manakala $\text{La-CuFe}_2\text{O}_4$ mempunyai ketumpatan 3.4734 g/cm^3 . CuFe_2O_4 menunjukkan sifat pemangkin yang lebih bagus, iaitu isi padu pora sebanyak $0.1683 \text{ cm}^3/\text{g}$ dan luas permukaan sebanyak $102.37 \text{ m}^2/\text{g}$. XRD membuktikan CuFe_2O_4 wujud dalam kristal padu berpusat muka. Foto degradasi 0.5 v/v % gliserol dengan sumber cahaya nampak dari lampu Xenon (panjang gelombang 400-700 nm) dengan ferit tembaga (Cu 30 wt %) dan kuprum ferit didopan dengan lantanum (La 40 wt %) telah dijalankan untuk menentukan keberkesanannya. Jumlah hidrogen peroksida (H_2O_2) ditambah untuk mewujudkan sistem Fenton telah diubah untuk mengkaji kesan H_2O_2 dalam keberkesanan fotopemangkinan. CuFe_2O_4 tanpa pendopan berkesan merendahkan kepekatan metilena biru dalam penemuan awal, tetapi kesan fotopemangkinan tidak signifikan terhadap gliserol. Keputusan menunjukkan bahawa H_2O_2 0.5 mL dan ke atas menyebabkan degradasi gliserol, manakala 1.0 mL H_2O_2 ke atas diperlukan untuk degradasi gliserol dengan $\text{La-CuFe}_2\text{O}_4$. Kadar dan tahap degradasi gliserol meningkat dengan jumlah H_2O_2 . Oleh itu, kajian ini telah membuktikan bahawa CuFe_2O_4 boleh merendahkan konsentrasi gliserol bawah sumber cahaya nampak dalam tindak balas photofenton.

TABLE OF CONTENTS

SUPERVISOR'S DECLARATION	IV
STUDENT'S DECLARATION	V
Dedication	VI
ACKNOWLEDGEMENT	VII
ABSTRACT	VIII
ABSTRAK	IX
TABLE OF CONTENTS	X
LIST OF FIGURES	XII
LIST OF TABLES	XIV
CHAPTER 1	1
1 INTRODUCTION	1
1.0 Introduction	1
1.1 Motivation and statement of problem	2
1.2 Objective	3
1.3 Scope of research	3
1.4 Main contribution of this work	4
CHAPTER 2	5
2 LITERATURE REVIEW	5
2.0 Overview	5
2.1 Introduction	5
2.2 Glycerol	6
2.3 Glycerol from Biodiesel Synthesis	6
2.4 Glycerol Degradation	8
2.5 Photocatalysts	8
2.6 Dopant	11
2.7 Fenton-System	12
2.8 Photocatalysis of Glycerol	13
2.9 Copper Ferrite Photocatalyst	14
2.10 Summary	18
CHAPTER 3	19
3 METHODOLOGY	19
3.0 Introduction	19
3.1 Chemicals	19
3.2 Photocatalyst Preparation	20
3.3 Characterization	21
3.3.1 Helium Displacement	21
3.3.2 Nitrogen Physisorption	23
3.3.3 Field Emission Scanning Electron Microscopy (FESEM)	26
3.3.4 X-Ray Diffraction (XRD)	27
3.4 Preliminary Study: Methylene Blue Photodegradation	30
3.5 Glycerol Photodegradation	32
3.6 Sample Analysis	33
3.6.1 UV-Vis Spectrophotometer	33
3.6.2 High Performance Liquid Chromatography (HPLC)	35
3.7 Summary	39

CHAPTER 4	40
4 RESULTS AND DISCUSSION	40
4.0 Introduction	40
4.1 Catalyst Characterization	40
4.1.1 Helium Displacement ²	40
4.1.2 Brunauer-Emmett-Teller (BET)	42
4.1.3 Field Emission Scanning Electron Microscope (FESEM)	45
4.1.4 X-Ray Diffraction (XRD)	48
4.2 Photocatalytic Activity Testing with Methylene Blue Solution	50
4.3 Glycerol Photodegradation	52
4.4 Kinetics of Glycerol Photodegradation over Copper Ferrite	57
CHAPTER 5	61
5 CONCLUSION AND RECOMMENDATIONS	61
5.1 Conclusion	61
5.2 Recommendations	62
REFERENCES	63
APPENDICES	68

LIST OF FIGURES

Figure 2-1: Structure of Glycerol.....	6
Figure 2-2: Transesterification process.....	7
Figure 2-3: Mechanism of photo-reforming of methanol over ferrite photocatalyst.....	10
Figure 2-4: Mechanism of glycerol degradation over TiO ₂ catalyst.....	14
Figure 2-5: The effect of copper ferrite loadings on photocatalytic ozonation of RR198.	15
Figure 2-6: Removal Efficiency of Imidacloprid in presence of CF, peroxide, leaching+peroxide and fenton system.....	16
Figure 2-7: The Effect of Copper Ferrite Loadings on Atrazine Degradation.	16
Figure 2-8: Photodegradation of 20 ppm methylene blue over copper ferrite under visible light.	17
Figure 3-1: Pycnometer type 1305 Micromeritics.....	23
Figure 3-2: Isotherm of BET adsorption.....	24
Figure 3-3: Thermo scientific Surfer	25
Figure 3-4: Schematic Diagram of FESEM.....	26
Figure 3-5: JEOL JSM-7800F FESEM.	27
Figure 3-6: Rigaku Miniflex II.	29
Figure 3-7: Schematic Diagram of XRD.	29
Figure 3-8: Xenon lamp housing of photoreactor.....	31
Figure 3-9: Addition of catalyst into the larger diameter housing of photoreactor containing methylene blue solution.	31
Figure 3-10: Set up during the experiment.	32
Figure 3-11: Hitachi U-1800 Spectrophotometer.	34
Figure 3-12: Mechanism of UV-Vis Spectrophotometer	35
Figure 3-13: The Operating Parts of HPLC.....	36
Figure 3-14: Agilent HPLC Series 1200.....	37
Figure 3-15: Zorbax Carbohydrate HPLC column.	37
Figure 4-1: Graph of Density vs Time of copper ferrite catalyst from gas pycnometer.	41
Figure 4-2: Isotherm of copper ferrite from BET analysis.	43
Figure 4-3: Surface area of copper ferrite by 2 Parameters Line from BET analysis. ...	44
Figure 4-4 (a): FESEM image of copper ferrite before calcination at 5,000 times magnification.	45
Figure 4-4 (b): FESEM image of copper ferrite before calcination at 30,000 times magnification.	46
Figure 4-4 (c) FESEM image of copper ferrite before calcination at 50,000 times magnification.	46

Figure 4-5 (a): FESEM image of copper ferrite after calcination at 5,000 times magnification.	47
Figure 4-5 (b): FESEM image of copper ferrite after calcination at 30,000 times magnification.	47
Figure 4-5 (c): FESEM image of copper ferrite after calcination at 50,000 times magnification.	478
Figure 4-6: XRD pattern of copper ferrite.	49
Figure 4-7: Graph of C/Co versus time for methylene blue photocatalytic degradation, photo-Fenton degradation and blank run	51
Figure 4-8: Photocatalytic effect on methylene blue (increasing time from left to right).51	
Figure 4-9: Chromatogram of glycerol at t=0 min in photodegradation over 2.0 g/L copper ferrite and 0.1ml hydrogen peroxide.....	52
Figure 4-10 (a): Normalized concentration of glycerol for photodegradation over 2.0 g/L copper ferrite with various hydrogen peroxide loadings.	54
Figure 4-10 (b): Normalized concentration of glycerol for photodegradation over lanthanum doped copper ferrite with various hydrogen peroxide loadings.....	55
Figure 4-10 (c): Comparison of photocatalytic activity of copper ferrite with and without lanthanum dopant with 1.0 mL H ₂ O ₂	56
Figure 4-11: Zero order linear plot of glycerol photodegradation over copper ferrite catalyst.	58
Figure 4-12: First order plot of glycerol photodegradation over copper ferrite catalyst.59	
Figure 4-13: Second order plot of glycerol photodegradation over copper ferrite catalyst.	60

LIST OF TABLES

Table 2-1 Previous photocatalytic research results on various photocatalysts.....	9
Table 2-2 Previous lanthanum dopant results on various photocatalysts.	11
Table 3-1: List of chemicals needed	20
Table 3-2 Equipment for catalyst characterization techniques	21
Table 4-1: Mass of catalysts.	40
Table 4-2: Gas pycnometer density results of copper ferrite catalyst.....	41
Table 4-3: Gas pycnometer density results of copper ferrite catalyst doped with lanthanum.....	42
Table 4-4: BET analysis results for copper ferrite catalyst with and without lanthanum dopant.....	44
Table 4-5: Analysis of peaks from XRD pattern of copper ferrite.	50
Table 4-6: Normalized concentration of glycerol (C/Co) after 4 h degradation	53
Table 4-7: Normalized concentration of glycerol (C/Co) after 4 h degradation	53
Table 4-8: Values utilized to develop the kinetics of glycerol photodegradation over copper ferrite.....	58

CHAPTER 1

1 INTRODUCTION

1.0 Introduction

Fossil fuel is essential for energy generation to support various existing industries, transportation operation as well as for daily routine. Over the decades, petroleum, oil and coal have been employed as energy sources through combustion to cope for the energy demand of humankind. Substitutes to these resources have been eagerly discovered due to the environmental degradation led by their indiscriminate burning, and their non-renewability, fuels and costly to obtain.

Biodiesel, an agricultural-based liquid transportation substitute, consists of simple alkyl ester groups derived from agricultural fats and oils, which ranged from plant oils, animal fats to edible waste processing oils. Due to its renewability and energy generation efficiency comparable to the traditional non-renewable resources, biodiesel has attracted growing attention. This can be seen by the production increment to meet the consumption and demand. In Malaysia itself, biodiesel production approved in March 2010 has reached 6.8 million tonnes (Dompok, 2010).

Significantly, glycerol is a side product from the transesterification process to produce biodiesel. Consequently, glycerol production increases proportionally with the rise in biodiesel production. However, the purification of glycerol produced to USP grade is expensive and thus disposal is the often option in Malaysia and many other countries (Haas et al., 2006). The current work aims to explore the degradation of glycerol waste which might be harmful to the environment in high quantity.

The reaction to degrade the waste glycerol will be achieved over a photocatalyst, in this study, copper ferrite catalyst. This catalyst has the characteristics to perform photocatalytic activity under visible light.

1.1 Motivation and Statement of Problem

Glycerol is a commonly obtained side product from the transesterification of vegetable oil with methanol (Haas *et al.*, 2006). Biodiesel demand is on the rise following the economic boom especially in developing countries such as India and China. World biodiesel capacity from 2002 to 2008 has far exceeded the production, and thus biodiesel production continues to increase exponentially to meet the growing demand (Biodiesel 2020: A Global Market Survey, 2nd Edition, 2008). In Malaysia, biodiesel in the forms of B5 and B10 have been adopted as transportation fuel. Thus glycerol, the side products will also increase correspondingly.

At the local front, due to the lack of handling and processing industries, the environmental regulations in Malaysia have classified glycerol as waste under Schedule S181. The economic potential of glycerol is unknowingly denied where it is stored in drums and eventually disposed in landfills (Hidawati & Sakinah, 2011). Instead of disposal, this glycerol can be converted into hydrogen, which is a non-polluting energy source. Hydrogen combustion to generate energy produces only water as the product of reaction. Current hydrogen production in industries is mainly from the steam reforming, which uses natural gas (47%), oil (30%), and coal (19%) as the raw materials (Nichele *et al.*, 2014). Unfortunately, this thermal reaction of hydrocarbon consumes large amount of heat energy and emits greenhouse gasses which leads to climate change (Nowotny *et al.*, 2014). Significantly, an economic and more eco-friendly method to produce hydrogen is via photodegradation of glycerol. In this method, the products of the reaction are hydrogen/ syngas, which are all efficient fuels for energy generation. In addition, photocatalysis utilizes readily available light energy, which is practical for a sun-drenched country like Malaysia.

Previous and ongoing studies of photocatalysis are abundant, ranging from the simple metal oxides such as TiO_2 to complicated catalyst systems such as fenton-system, with the former being the most common. However, the large band gap of TiO_2 (3.0 eV) renders the material only active under the UV light (Hashimoto *et al.*, 2005). Indeed, band gap of a catalyst determines the wavelength of light energy to be absorbed. The wider the band gap, the lower the range of absorbable wavelength. Hence, it is more practical to synthesize a photocatalyst which can absorb visible light (wavelength range from 400 to 700 nm) because visible light represents the widest range of solar spectrum.

Consequently, this study is carried out to determine the physicochemical properties of ferrite doped with copper. Significantly, copper ferrite (CuFe_2O_4) is employed due to

its narrow band gap (~ 1.32 eV) as opposed to the other near similar systems *i.e.* CaFe_2O_4 , MgFe_2O_4 , ZnFe_2O_4 and NiFe_2O_4 .

Previous studies with photocatalysts show higher oxidation activity with lanthanum, La, as dopant, due to the decrease in the oxygen vacancies, which acts as the sites for electron-hole recombination. In other words, La dopant decreases the rate of deactivation of the CaFe_2O_4 catalyst, thus giving a higher photocatalytic activity in a reaction (Masahiro, 2004). Therefore, CuFe_2O_4 doped with lanthanum, La will also be investigated for its catalytic activity.

1.2 Objective

This research aims to synthesize and characterize the physicochemical properties of copper ferrite, CuFe_2O_4 with and without lanthanum dopant, $\text{La-CuFe}_2\text{O}_4$, for photocatalytic degradation of glycerol solution.

1.3 Scope of Research

In order to achieve the objectives of the current work, the following scopes have been identified:

- i. To synthesize a CuFe_2O_4 photocatalyst with metal loading of 30 wt %, with and without La dopant (40 wt %), using co-precipitation method.
- ii. To characterize the physicochemical properties of CuFe_2O_4 photocatalyst using the following analyses:
 - a) Helium displacement method
 - b) Nitrogen (N_2) physisorption
 - c) Field Emission Scanning Electron Microscopy (FESEM)
 - d) X-ray diffraction (XRD)
- iii. To study the kinetics of the photodegradation of 5 v/v % glycerol solution over CuFe_2O_4 and $\text{La-CuFe}_2\text{O}_4$ via varying hydrogen peroxide, H_2O_2 loadings (photo-Fenton system).

1.4 Main contribution of this work

This study demonstrates the application of copper ferrite (CuFe_2O_4) and copper ferrite doped with lanthanum ($\text{La-CuFe}_2\text{O}_4$) on glycerol photodegradation into hydrogen gas. This provides a method to degrade glycerol for disposal.

CHAPTER 2

2 LITERATURE REVIEW

2.0 Overview

This chapter presents the experimental studies of photodegradation of glycerol into hydrogen gas over copper ferrite (CuFe_2O_4) and copper ferrite doped with lanthanum ($\text{La-CuFe}_2\text{O}_4$) using Xenon light as visible light source. Previous studies of photocatalysis focus more on UV light as the activation energy source. Common photocatalyst such as TiO_2 has a band gap too wide to be activated by visible light which has lower energy than UV spectrum. Copper ferrite is known to have a relatively narrow band gap, enough to be activated by energy from visible light spectrum. Moreover, the net rate of activation is known to be increased by lanthanum dopant, in other photocatalysts such as SrTiO_3 . La is therefore doped on CuFe_2O_4 with expected rise in photocatalytic activity. Hydrogen peroxide (H_2O_2) added to the photocatalysis reaction creates a photo-Fenton system which enhance rate of photocatalytic reaction.

2.1 Introduction

Glycerol is produced from transesterification process to obtain biodiesel. Glycerol from the by-product of this process is being focused in this study to explore its potential to produce hydrogen as clean and efficient fuel despite being treated as industrial waste. Current treatment applied to the glycerol from biodiesel industries and a number of proposed treatment are reviewed in this chapter. The potential of photocatalysis in treating glycerol is justified, supported by photocatalysis of other similar organic compounds. This chapter summarize the results of previous studies regarding photocatalytic reactions and catalytic activities of ferrites photocatalysts.

2.2 Glycerol

Glycerol is the common name for the compound 1,2,3-propanetriol. It is a viscous liquid at room temperature and pressure, and is colourless, odorless and has a sweet taste. Glycerol is highly soluble in water and alcohols, but is insoluble in hydrocarbons. The three hydrophilic hydroxyl groups enable it to be soluble in water and endow it with hygroscopic property. It forms intra and intermolecular hydrogen bonds, thus having high solubility in water and other solvents (Brown *et al.*, 2012).

Figure 2-1 shows the skeletal structure of glycerol.

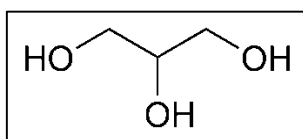


Figure 2-1: Structure of Glycerol

2.3 Glycerol from Biodiesel Synthesis

Biodiesel fuel has gained its recognition as good substitute of non-renewable fuels in various aspects in recent years. Due to the raising concern to the environment and the deplete of fossil fuels unable to sustain for future use, biodiesel which has the energy efficiency compatible with fossil fuels has become an alternative fuel in many countries. Despite resolving the problem of future shortage of fossil fuels, biodiesel combustion releases less amount of pollutants as compared to the fossil fuels such as petroleum diesel. The products from energy generation by biodiesel combustion contain relatively lower levels of sulphur and aromatics (Rocha *et al.*, 2014).

Biodiesel, as previously mentioned, is produced through the transesterification of agricultural oil (plant oil or animal fat) and short chain alcohols (usually methanol) over a homogeneous or heterogeneous catalyst (Rocha *et al.*, 2014). Among the common homogeneous catalysts, are sodium hydroxide and potassium hydroxide (Ang *et al.*, 2014). From the chemical reaction, biodiesel will be yielded, with glycerol as the undesired side product (Rocha *et al.*, 2014). The reaction of biodiesel production can be illustrated in Figure 2-2.

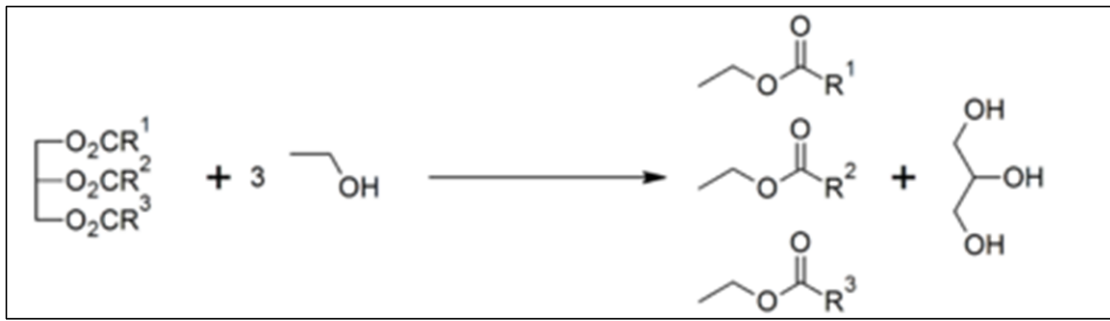


Figure 2-2: Transesterification process.

As reported by Pagliaro and Rossi (2010),



This chemical reaction shows that glycerol accounts for approximately 10% by volume of the product (Rocha *et al.*, 2014).

According to Pagliaro and Rossi (2010), every 100 kg of biodiesel production yields more than 10 kg of glycerol (cf. (2-1)). Palm oil biodiesel alone in Malaysia is produced at a rate of 3.93 ton per year, leaving about 0.4 ton of glycerol being treated as a scheduled waste in Malaysia.

Due to the advantages contributed by biodiesel, the biodiesel market increases exponentially in the recent years. It is estimated that the global biodiesel market could reach up to 37 billion gallons by 2016, considering an annual growth demand of 42% from current available statistics (Anand & Saxena, 2012). This demand-production phenomena has resulted in flooding of glycerol into the market, thus causing a glut of glycerol. From 2002 to 2009, the price of glycerol has fallen 20-fold to approximately \$0.10/kg, and the trend continues to decline (Johnson & Taconi, 2009).

Glycerol from biodiesel production is mostly treated as scheduled waste, due to economic reasons and its properties. Since glycerol is a hydrocarbon compound, it can be burned to generate energy. However, the heat value is too low that the process does not result in relevant economic potential (Sims, 2011). Moreover, glycerol from biodiesel production is contaminated with unreacted reactants or trace amount of side products, such as saponified fatty acids (SFAs) and methanol (Pott *et al.*, 2014). Such contamination requires complicated processes to supply for consumer market. Treatment to pharmaceutical grade is even more unsuitable to be considered when high temperature low pressure distillation has to be employed to purify the glycerol. Therefore, glycerol is

disposed as scheduled waste since the purification processes are uneconomical for this low cost commodity (Pagliaro & Rossi, 2008).

2.4 Glycerol Degradation

Previous catalytic studies indicate that reforming of glycerol can produce H₂ and CO (Tran & Kannangara, 2013), collectively also known as syngas, which is a sustainable source of energy. Many studies have been carried out on aqueous phase reforming of glycerol to produce hydrogen gas, which is more efficient and convenient as compared to hydrogen production by steam reforming of natural gas (Pagliaro & Rossi, 2010). Nonetheless it requires high pressure and elevated temperature, in total contrast to the current proposition which only utilizes ambient operating conditions and light-activation mechanism, hence more attractive.

Degradation of glycerol via biomechanisms are also published. Among the papers, Sabourin-Provost and Hallenbeck (2009), has reported hydrogen production method using photofermentative bacterium *Rhodospseudomonas palustris*. This has been the most prominent biomechanism adapted in hydrogen production from glycerol. The bacterium has been known for decades for its hydrogen yielding from organic substrates, but glycerol has just been demonstrated as the substrate recently at 2009. Prior to that, organic acid has been more commonly investigated as the substrates. (Pott *et al.*, 2013)

2.5 Photocatalysts

Photocatalysts have semiconductor properties in which the electrons can be promoted to a higher energy level when being activated by light energy ($h\nu$), thus creating an activated electron and a positively charged hole. The larger the band gap, the more energy, and thus the light energy of shorter wavelength is required to promote the electron (Hashimoto *et al.*, 2005). Therefore, photocatalyst with large band gap, such as TiO₂ (band gap of 3.0eV) requires high energy, or short wavelength to activate its photocatalysis characteristics. Therefore it is more suited for UV light (wavelength of 300 to 400 nm). To be able to absorb visible light which makes up the widest range of wavelength, band gap of the photocatalyst must not exceed 3.1 eV. Certain dopants,

including metal, nitrogen, carbon, and combination of those, can narrow the band gap of photocatalysts.

Spinel ferrites, or metal ferrites, with formula MFe_2O_4 where M is a metal cation, is an effective photocatalyst under visible light due to its narrow band gap ranging from 1.32 to 2.19 eV. Among few common spinel ferrites, $CuFe_2O_4$ has the lowest band gap of 1.32 eV. Moreover, spinel ferrites have a crystal structure which possesses extra catalytic sites to enhance the catalytic efficiency.

Table 2-1 shows the photocatalytic activities of ferrites in degrading different concentrations and types of dyes, in which $ZnFe_2O_4$ and $SiO_2/NiFe_2O_4$ showed relatively low degradation. In contrast, $CuFe_2O_4$ nanoparticles showed effective degradation of *reactive red* under UV light. $CoFe_2O_4$ doped with graphine and $LaFeO_3$ nanoparticles degrade the dyes well under visible light.

Table 2-1 Previous photocatalytic research results on various photocatalysts.

Catalyst	Reactant	Catalyst loading	Irradiation source	Irradiation time (min)	Degradation (%)	References
$BaFe_2O_4$	20 mg/L methyl orange	5.0 g/L	UV	120	35-90	(Yang, <i>et al.</i> , 2007)
$CoFe_2O_4/ZnO$	50 mg/L methyl orange	30 g/L	UV	300	93.9	(Zhang <i>et al.</i> , 2009)
$SiO_2/NiFe_2O_4$	10 mg/L methyl orange	1.0 g/L	$\lambda < 400$ nm	60	5	(Xu <i>et al.</i> , 2007)
$Bi_{12}TiO_{20}/NiFe_2O_4$	10 mg/L methyl orange	1.1 g/L	$\lambda < 400$ nm	60	52	(Xu <i>et al.</i> , 2007)
$ZnFe_2O_4$	25 mg/L methyl orange	5.0 g/L	$\lambda < 400$ nm	240	4	(Cheng <i>et al.</i> , 2007)
$CoFe_2O_4-G(0.4)$	100 mg/L methylene blue	0.3 g/L	Visible light	240	90	(Fu <i>et al.</i> , 2012)

LaFeO ₃ NPs	TBO dye in aqueous solution	0.18 g/L	Visible light	90	98	(Abazari <i>et al.</i> , 2014)
CuFe ₂ O ₄ nanoparticles	150 mg/L reactive red (RR198)	0.03	UV	12	95	(Mahmoodi & Mohammad, 2011)

Photocatalysts are commonly utilized to degrade organic substances. The products of photocatalysis of organic substance are commonly carbon dioxide or carbon monoxide, and hydrogen gas. Previous studies utilized organic dyes as reactants to study the activities of photocatalysts. Examples include methyl orange dye (Wei *et al.*, 2004), methylene blue solution (Fu *et al.*, 2012) and TBO dye (Abazari *et al.*, 2014). Other organic substances studied for photocatalytic reactions include methanol (Lv *et al.*, 2010) and propanol (Masahiro *et al.*, 2004). The mechanism of photo-reforming of methanol illustrated in Figure 2-3 is an example of the photodegradation mechanism of organic substances.

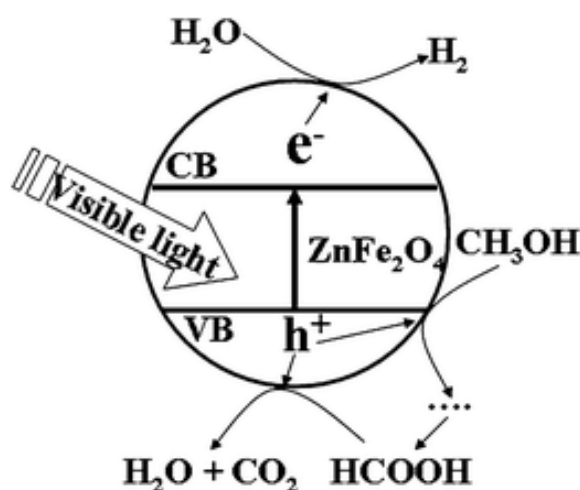


Figure 2-3: Mechanism of photo-reforming of methanol over ferrite photocatalyst. (Lv H. *et al.*, 2010)

2.6 Dopant

Most photocatalysts are active only under UV light irradiation due to the wide band gap activated only by high energy in the UV spectrum. To shift the optical response, an approach is to dope the catalyst with one or more other element(s). Common dopants like nitrogen, carbon and silicon, or combination of such, have proven to improve catalytic activities. (Casbeer *et al.*, 2012) Heavy metals, when doped with TiO₂ enable the photocatalysts to be active under visible light. Experimented metals include cobalt (Hsieh *et al.*, 2009), silver (Zielinska *et al.*, 2010), gold (Luo *et al.*, 2011), platinum (Li *et al.*, 2008) and ruthenium (Senthilnathan *et al.*, 2010).

Lanthanum dopant has also been studied and showed significant improvement in photocatalytic activities, as summarized in Table 2-2.

Table 2-2 Previous lanthanum dopant results on various photocatalysts.

La content	Catalyst	Reaction	Result without La	Result with La	Ref.
0.5%	SrTiO ₂	Propanol → acetone + hydrogen	Acetone generation = 0.01ppm/min	Acetone generation = 0.07ppm/min	(Masahiro <i>et al.</i> , 2004)
2%	NaTaO ₃	H ₂ and O ₂ evolution from aqueous NaOH	H ₂ =10.3mmol/h O ₂ =0.78mmol/h	H ₂ =13.2mmol/h O ₂ =1.7mmol/h	(Kato <i>et al.</i> , 2003)
0.5%	TiO ₂	Degradation of methyl orange	C/C ₀ = 0.6	C/C ₀ = 0.45	(Wei <i>et al.</i> , 2004)
0.5% (with N550)*	TiO ₂	Degradation of methyl orange	C/C ₀ = 0.6	C/C ₀ = 0.1	(Wei <i>et al.</i> , 2004)

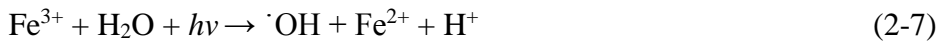
*N550 indicates nitrogen dopant by annealing with NH₃ at 550°C.

2.7 Fenton-System

Oxidizing agent, such as H₂O₂ are added into the ferrite system to enhance the photocatalytic activity, thus creating a Fenton system. The series of reactions between iron ions and H₂O₂ proceeds to produce free radicals from water molecules, namely $\cdot\text{OH}$ and $\cdot\text{OOH}$. The reactions can be illustrated by Equations (2.2) through (2.6). (Casbeer *et al.*, 2012)



Fenton system, when combined with the presence of light, results in photo-Fenton system. In addition to Equation (2-2) to (2-6), Equation (2-7) occurs to contribute to higher formation rate of $\cdot\text{OH}$ free radicals.



Light irradiation also promotes the recycling of ferrite catalyst through the reduction of Fe³⁺ to Fe²⁺. Consequently, the higher concentration of Fe²⁺ increases the rate of photocatalytic reaction. (Tamimi *et al.*, 2008)

Besides photo irradiation, electrochemical process is another factor to accelerate the redox cycle of Fe²⁺/Fe³⁺ and the generated $\cdot\text{OH}$ (Fukuchi *et al.*, 2014).

Even though reducing agent can effectively accelerates the reduction of Fe³⁺ to Fe²⁺, the oxidation of the reducing agent by $\cdot\text{OH}$ is a competition to the photocatalysis degradation in the Fenton system. In this case, the reducing agent acts as a competitive inhibitor of the main process. However, reducing agents such as ascorbic acid and hydroxylamine are reported to effectively enhance the generation of $\cdot\text{OH}$ and then degrade organic substances at higher activity (Fukuchi *et al.*, 2014).

Copper can also catalyze the conversion of H₂O₂ to produce hydroxyl radicals, $\cdot\text{OH}$ via a Fenton-like reaction. Copper ferrite photocatalyst, CuFe₂O₄ provides the copper for this reaction. While the catalytic activity of iron ion, Fe²⁺ is higher at acidic conditions, copper catalyzes the reactive oxidants formation with higher activity at

circumneutral and alkaline pH conditions. The increased catalytic activity of copper at such conditions is contributed by the higher solubility of copper ions at high pH. Cupryl ion, Cu^{3+} produced outperform $\cdot\text{OH}$ as oxidants at neutral pH conditions, even though the reactivity with compounds is not well investigated (Lee *et al.*, 2014).

The hydroxyl free radicals produced is proven effective in destructing organic pollutants, therefore has been applied for organic waste treatment in industries. The production of free radicals speed up the reaction by providing readily available sites for binding during the photocatalytic degradation (Ding *et al.*, 2014). In other words, the addition of H_2O_2 to create Fenton system provides a higher rate of photocatalytic reactions over ferrites.

2.8 Photocatalysis of Glycerol

Similar to other photocatalytic reactions, photocatalysis of glycerol proceeds from the activation of solid catalyst by promotion of electron through the band gap to the valence band, resulting in an electron, e^- and a positively-charged hole, h^+ to perform the redox reaction.

In all routes, glycerol degradation produces hydrogen gas as the products. The balanced equation of glycerol degradation in form of aqueous solution is shown in Equation (2-8).



Since the reaction is photocatalytic reaction instead of photo-oxidation reaction, it can take place in unaerated condition, implying that no additional oxygen is needed to oxidize the reaction. In such photocatalytic reaction, the holes generated from the light energy is utilized to oxidize the organic compound. The corresponding electrons produced in pair with the holes reduce water to hydrogen gas (Panagiotopoulou *et al.*, 2013). The reaction mechanism can be shown by Figure 2-4, having TiO_2 as the photocatalyst and glycerol as the reactant, as a sample illustration of anticipated mechanism over ferrite photocatalyst in the current work. Photocatalysis of glycerol proceeds with the same mechanism despite the photocatalysts used. The products of glycerol photo reforming hydrogen gas (Tran & Kannangara, 2013).

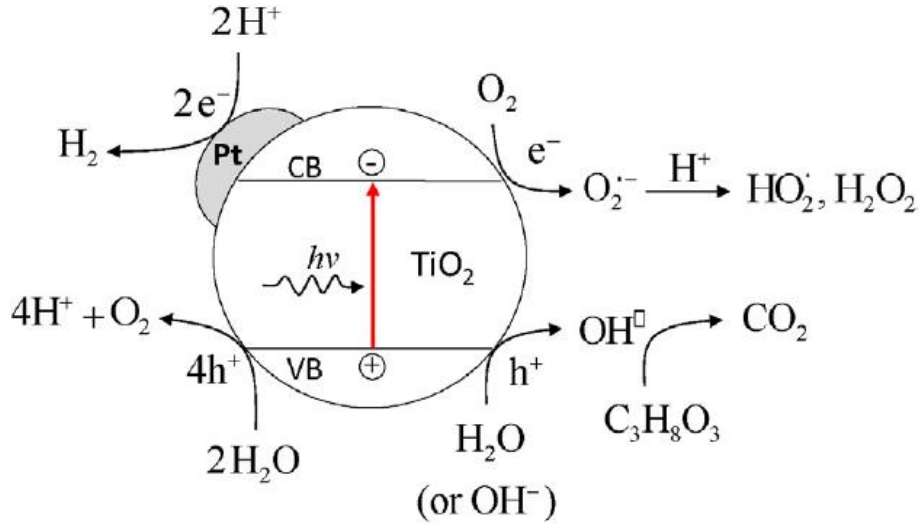


Figure 2-4: Mechanism of glycerol degradation over TiO₂ catalyst.

2.9 Copper Ferrite Photocatalyst

Copper ferrite photocatalyst, CuFe₂O₄ is a type of spinel ferrite. Due to its low band gap energy of 1.32 eV, the photocatalysis is active at low wavelengths. From Equation (2-9), the wavelength by which copper ferrite is active under is less than 939 nm. This means that copper ferrite photocatalyst is active under visible light with wavelength of 390 to 780 nm besides UV irradiation.

$$\text{Wavelength, } \lambda \text{ (nm)} \leq 1240/\text{Band gap of semiconductor (eV)} \quad (2-9)$$

Copper ferrite photocatalyst has been studied in various systems, such as Fenton system, peroxymonosulphate catalysed, and ozonation. These additions to the photocatalyst aim to enhance the photocatalytic activities by increasing the rate of photocatalysis. The oxidation species added form free radicals, thus aiding the mechanism of the reaction.

Mahmoodi (2011) presents photocatalytic ozonation of Reactive Red (RR 198 and RR 120) using copper ferrite under UV irradiation. The photodegradation rates under different catalyst loading are shown in Figure 2-5.

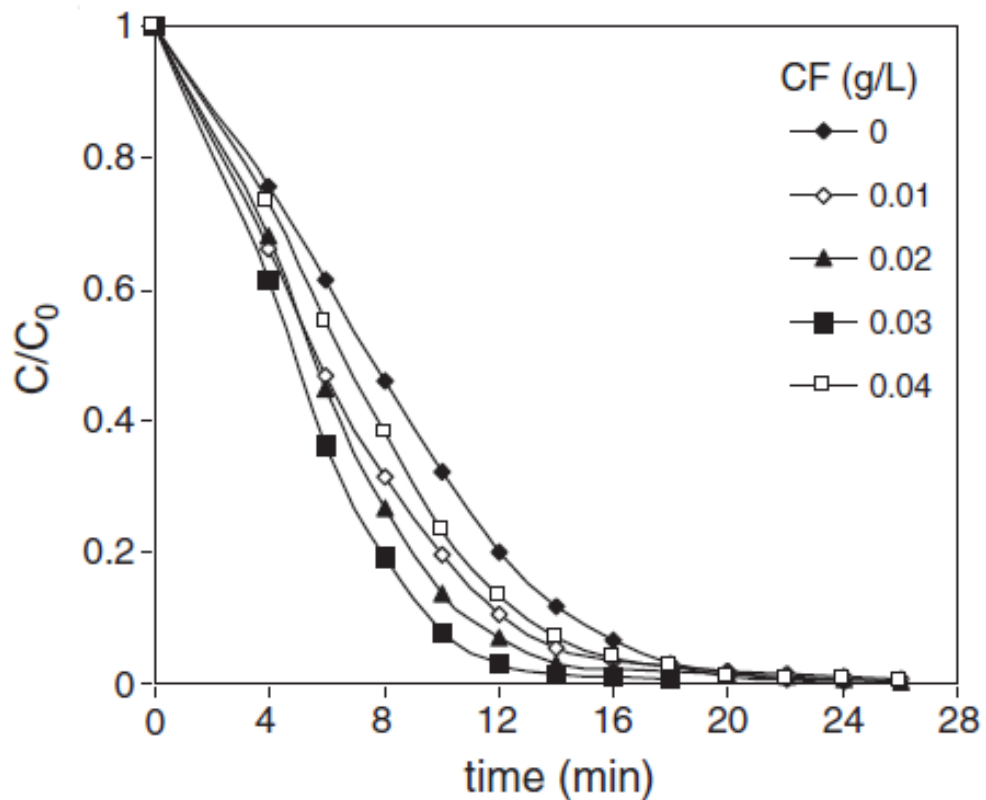


Figure 2-5: The effect of copper ferrite loadings on photocatalytic ozonation of RR198. (Mahmoodi, 2011)

Copper ferrite has been added with hydrogen peroxide to create fenton system. In the study of imidacloprid degradation by fenton system, it is found out that the amount of free radicals generated is directly proportional to the degradation of imidacloprid (Wang *et al.*, 2014). The effectiveness of the copper ferrite fenton system in the mentioned reaction is shown in Figure 2-6.

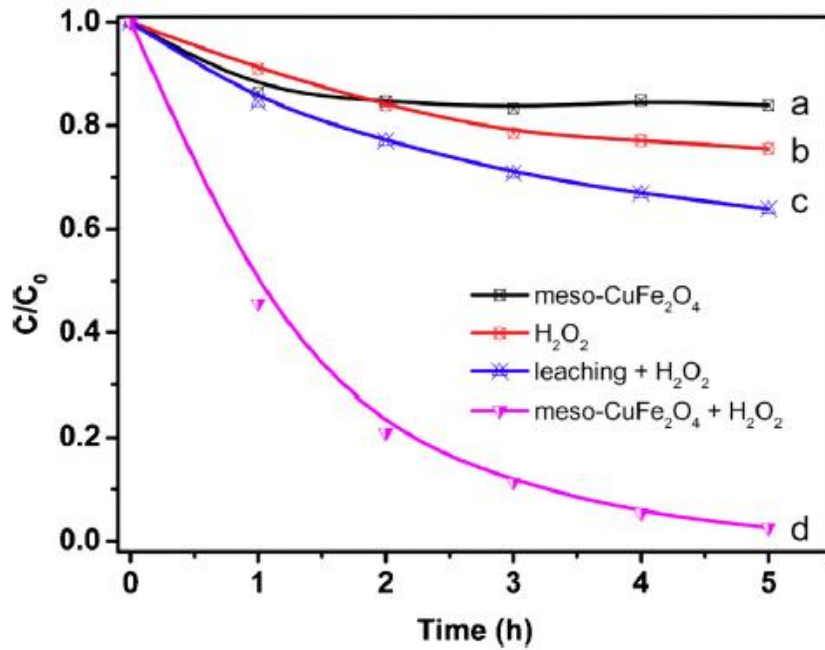


Figure 2-6: Removal efficiency of imidacloprid in presence of CF, peroxide, leaching+peroxide and Fenton system. (Wang et al., 2014)

Peroxymonosulfate provides formation of hydroxyl and sulfate radicals. Figure 2-7 presents the results from the study of degradation of atrazine by copper ferrite catalyzed peroxymonosulfate oxidation (Guan *et al.*, 2013).

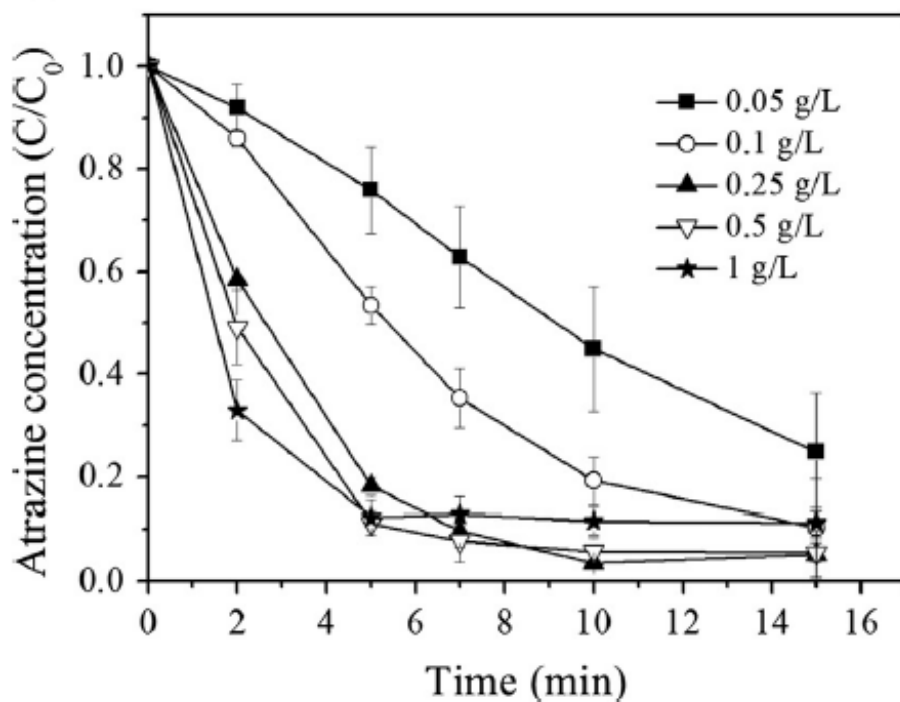


Figure 2-7: The Effect of Copper Ferrite Loadings on Atrazine Degradation.

According to the study of Uddin *et al.* (2014), photodegradation of 20 ppm methylene blue under visible light irradiation increases with copper ferrite loadings from 0.3 to 1.0 g/L, as shown in Figure 2-8. The decisive factors of the reaction are the active sites on the surface of photocatalyst and the light penetration. However, as photocatalyst loading exceeds the critical point, light penetration into the reactor is obstructed and thus less active radicals can be generated to catalyze the photodegradation. Besides, extremely high loadings of copper ferrite photocatalyst results in collision which deactivate the activated catalyst to the ground state (Yang, 2007).

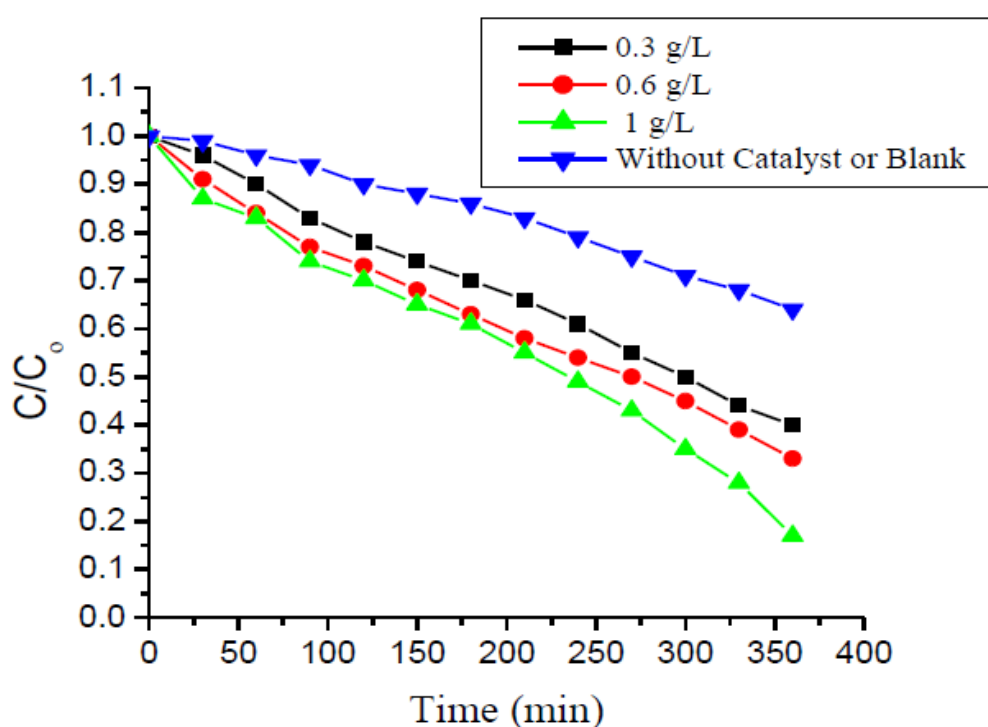


Figure 2-8: Photodegradation of 20 ppm methylene blue over copper ferrite under visible light.

In conclusion, copper ferrite has been studied for its catalytic activities for the degradation of various reactants. Most of the studies enhance the catalytic activities by aiding free radicals formation through the addition of oxidative compounds. Though copper ferrite has a narrow band gap to be activated by visible light spectrum, only UV irradiation has been studied. Therefore, in this research, the photocatalytic activity of copper ferrite catalyst under visible light irradiation will be studied.

2.10 Summary

This chapter presents the previous studies of glycerol from biodiesel synthesis, photocatalytic reactions of organic substances, and focuses on glycerol photocatalysis. From the studies, analysis is made for applying some improvement and modification to the previous findings of the reactions similar to this research.

CHAPTER 3

3 METHODOLOGY

3.0 Introduction

This chapter presents the preparation method of copper ferrite photocatalys, and copper ferrite doped with lanthanum. Furthermore, the analyses of the photocatalysts using various analytical equipment, *i.e.* helium displacement for gas pycnometer, nitrogen physisorption for Brunauer-Emmett-Teller (BET) analysis, X-Ray Diffraction (XRD) and Field Emission Scanning Electron Microscope (FESEM) are detailed in the subtopics of this chapter. The procedures of the photocatalytic reaction itself are explained in Sections 3.4 and 3.5, followed by the analysis of the experimental results. The analysis of the results includes the analysis of the methylene blue as the preliminary experiment result and the glycerol concentration.

3.1 Chemicals

The glycerol, copper (II) nitrate, iron (III) nitrate, lanthanum nitrate hexantrate and acetonitrile were all of analytical grade, and purchased from Sigma-Aldrich. Sodium hydroxide and hydrogen peroxide were of 10% and 30% purity, respectively, also purchased from Sigma-Aldrich. The gases, *i.e.* nitrogen/helium mixture, helium and nitrogen of highest purity were sourced from Air Products. The distilled water and ultra-purified water used throughout the experiment was obtained from water purification unit in the lab. The mentioned chemicals and their application are listed in Table 3-1.

Table 3-1: List of chemicals needed

Chemical	Purity	Application
Copper (II) nitrate, Cu(NO ₃) ₂	99%	Catalyst synthesis
Iron (III) nitrate, Fe(NO ₃) ₃	99%	Catalyst synthesis
Sodium hydroxide, NaOH	10%	Catalyst synthesis
Glycerol solution	99%	Photocatalytic reactant
Lanthanum nitrate hexanitate, La(NO ₃) ₃ ·6H ₂ O	99%	Catalyst dopant
Acetonitrile, CH ₃ CN (HPLC grade)	99%	HPLC analysis
N ₂ /He mixture	N ₂ =30.03%, He=balance	BET analysis
He	> 99.996%	BET analysis, density analysis.
N ₂	> 99.99%	BET analysis

3.2 Photocatalyst Preparation

The CuFe₂O₄ photocatalyst in the current work was prepared using co-precipitation method. Copper nitrate, Cu(NO₃)₂ and Iron (III) nitrate, Fe(NO₃)₃ of a mass ratio 1:2 were weighed carefully using an analytical balance of 4 decimal-places sensitivity. The weighed materials were dissolved in 100 ml distilled water and magnetic-stirred at high speed. After the copper nitrate and iron nitrate had fully dissolved in the water, 10% sodium hydroxide solution, NaOH was added drop by drop into the solution to raise the pH to 10 while the stirring continued for 30 minutes. The suspension was then heated to 95 °C to 100 °C for and maintained in the range for 2 h until a precipitate of copper ferrite nanoparticles, was obtained. It is important to measure the temperature of the mixture from time to time with a mercury thermometer to prevent overheating. The copper ferrite nanoparticles that formed were then washed repeatedly with distilled water (filter kit connected to a vacuum pump) until the water obtained from the filtration attained a pH 7.0. The filtered copper ferrite nanoparticles were transferred to a crucible to be oven-heated at 100 °C for 3 h followed by calcination at 900 °C for 3 h at 10 °C min⁻¹ increment.

Subsequently, the calcined catalyst was cooled to room temperature, then mortared to powder form and finally stored.

For catalyst doped with lanthanum (La), the salt precursor lanthanum nitrate hexantrate, $\text{La}(\text{NO}_3)_3 \cdot 6\text{H}_2\text{O}$ was added to the $\text{Cu}(\text{NO}_3)_2/ \text{Fe}(\text{NO}_3)_3$ aqueous solution. Then the aforementioned steps were repeated.

3.3 Characterization

Catalyst characterization was carried out to determine the physicochemical properties of the catalyst synthesized. From the results of characterization, information regarding various aspects of the physicochemical properties was obtained. Consequently, the physicochemical attributes in relation to the photocatalytic performance were analysed and understood. The catalyst produced is characterized by the methods listed in Table 3-2.

Table 3-2 Equipment for catalyst characterization techniques

Techniques	Equipment
He displacement	Pycnometer type 1305 Micromeritics
N_2 physisorption	Thermal Scientific Surfer
FESEM	JEOL JSM-7800F
XRD	Rigaku Miniflex II

The following subchapters describe the fundamental theory and concepts of the characterization techniques used in this research.

3.3.1 Helium Displacement

Gas pycnometer is an equipment to measure the density of solid particles through helium gas displacement technique. Density is defined as the ratio of mass to volume of a particle. Prior to the analysis by gas pycnometer, a sample needs to be weighed accurately to obtain the mass. The equipment basically measures the volume of the sample, and requires input of the sample mass to generate the result of the sample density. Helium displacement technique is particularly utilized to obtain the volume of particles with undefined geometry. The body of the particles displaces the fluid, *i.e.* helium gas,

when the helium gas was injected into the entire empty space within the pycnometer. From the volume of helium gas injected, the volume of the sample was directly determined based on the volume of displaced helium gas. This is based on the displacement principle from physical laws. Besides, helium gas, other non-adsorbing inert gas can also be used in the technique.

The primary principle of the operation of gas pycnometer is based on Boyle-Mariott law, as stated in Equation (3-1).

$$p_1 V_1 = p_2 V_2 = \text{constant} \quad (3-1)$$

where

p is pressure,

V is volume.

The density measured using a gas pycnometer is the particle density. Unlike bulk density which includes the pores within individual particles in addition to the inter-particle spacing, particle density measures only the volume displaced by the particle regardless of the spacing and pore volumes (Teipel, 2005).

The model of gas pycnometer used to determine the particle density of the catalysts was Pycnometer Type 1305 Micromeritics, as shown in Figure 3-1. For the analysis in this study, the gas pycnometer was set to run for three purges. The CuFe_2O_4 catalyst was weighed carefully and the mass was input into the software system. Then, the catalyst was inserted into the sample chamber. Finally, the system was left to run. The catalyst was removed when the pressure had relieved to atmospheric pressure after the analysis. The procedure was repeated for $\text{La-CuFe}_2\text{O}_4$.



Figure 3-1: Pycnometer type 1305 Micromeritics.

3.3.2 Nitrogen Physisorption

Nitrogen physisorption is the most widely used technique to determine the surface area of solid specimen. The application of this technique is based on the fact that surface atoms in solids attract surrounding gas molecules due to their electrical force imbalance. This phenomenon is called gas sorption. Physisorption is where the gas molecules are free to move around the sample surface, until a thin layer of adsorbate is formed to cover the entire solid surface as more molecules are introduced. From the number of molecules required to cover the solid surface in a monolayer, the surface area of the solid specimen is equal to the cross sectional area of the gaseous adsorbate.

The theory implied is the extension of Langmuir's pioneer work for monomolecular adsorption. Hypotheses based on Langmuir's theory are: gas molecules adsorb on solid surface in infinite layers; interaction between layers of adsorbed gas molecules does not exist; and Langmuir's theory is applicable to each layer of the gas molecules. The resulting Brunauer-Emmett-Teller (BET) equation derived is as shown in Equation (3-2).

$$\frac{P}{V(P_S - P)} = \frac{1}{cV_m} + \frac{(c-1)P}{cV_m P_S} \quad (3-2)$$

where

P =gas pressure

P_s = saturated pressure of the adsorbate gas

V =volume of gas adsorbed

V_m = volume of gas adsorbed corresponding to monolayer coverage

c = characteristic constant of the adsorbate

Figure 3-2 gives a sample of BET adsorption isotherm, where number of adsorbed particles increases with P/P_0 ratio.

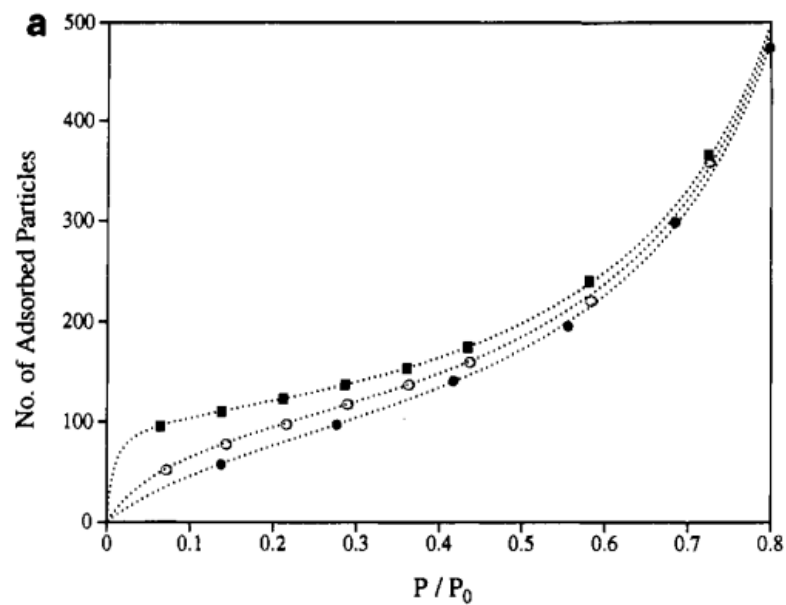


Figure 3-2: Isotherm of BET adsorption.

The BET instrument used in this research was Thermo scientific Surfer, as shown in Figure 3-3.



Figure 3-3: Thermo scientific Surfer

This model is fully automated to analyse the surface area and pore size of solid specimens. Prior to the analysis, it was ensured that the solid surface is free from contaminants so that it could be entirely layered by the gas molecules, N_2 . This was achieved by degassing, by heating the sample under vacuum condition. Then, the sample was preheated in the liquid nitrogen at 77 K. It is utilized with the aid of Autosorb software, AS1 WIN which offered the capability of using either branch of the isotherm for the pore size distribution calculation.

In the characterization of $CuFe_2O_4$ and $La-CuFe_2O_4$, the degassing temperature set for the BET was 300 °C. Liquid nitrogen was filled prior to the analysis. The density acquired from the gas pycnometer analysis was used as input for BET analysis. The settings were input and then the system was left to run until results were available.

3.3.3 Field Emission Scanning Electron Microscopy (FESEM)

Field Emission Scanning Electron Microscopy is a non-destructive analysis technique that is used to determine the sample morphology, topography, composition, crystalline structure and orientation of materials by directing a focused beam of high energy electrons to produce electrons emission from the surface of the sample.

The interaction between sample atoms and the bombarded electron beam results in signals regarding the sample's surface topography and composition. This can be achieved through secondary electron detection, which is a function of the angle between the sample surface and the beam. The narrow electron beam from the field-emission cathode in the electron gun contributes to a characteristic three-dimensional appearance of the sample surface. Since the image is produced by electron beam scanning, non-electrically conductive specimens may cause an accumulation of the electrostatic charge on the surface. Therefore, non-electrically conductive specimens are sometimes being coated with a layer of metal before the analysis. The mechanism of FESEM can be seen in Figure 3-4.

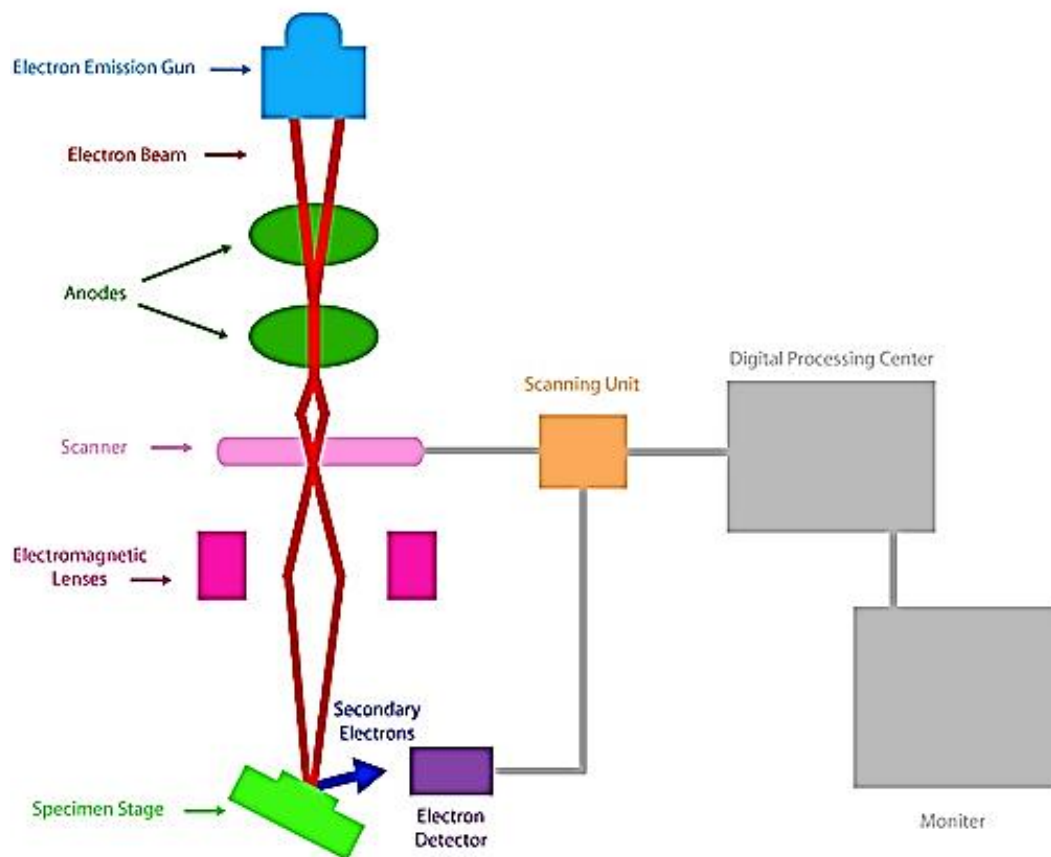


Figure 3-4: Schematic Diagram of FESEM.

JEOL JSM-7800F used to analyse the catalysts in this research is shown in Figure 3-5. It is able to provide image of up to 10^6 times magnification with 1 nm (at 15 kV) resolution. The electron beam sources from a thermally-assisted Schottky gun, which delivers long-term beam stability. Voltage accelerates at 10 V-30 kV. To overcome the problem of imaging for non-conductive matter, this model is capable of operation at low chamber vacuum (10-300 Pa). However for low vacuum analysis, the resolution drops to 1.5 nm.

In current work, CuFe_2O_4 was first coated with an extremely thin layer of gold-palladium to be made conductive for current. The Field Emission tip was utilized as the source of electrons. Next, the electron beam was focused by the electro-magnetic lenses and the apertures in the column to a tiny sharp spot. The image obtained was then saved.

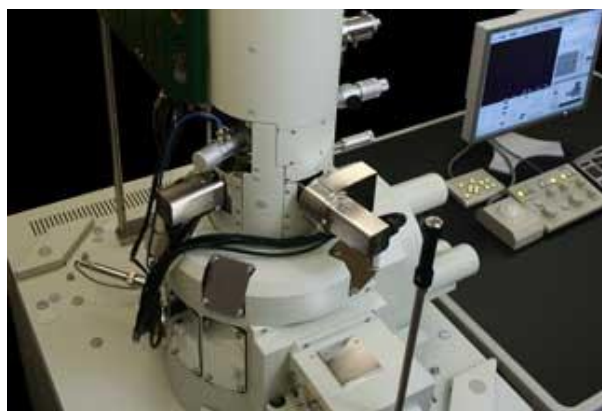


Figure 3-5: JEOL JSM-7800F FESEM.

3.3.4 X-Ray Diffraction (XRD)

X-Ray Diffraction technique is a non-destructive analysis widely used for the identification of structure, interatomic distances and bond angles. The results acquired from the analysis technique provides information of crystalline phases and sizes of crystallites. The analysed specimen can be in many forms, include powders, solids and ribbons, though powder form is more commonly applied. In addition, the amount required to carry out the analysis is as few as a few milligrams. However, greater amount of specimen up to a few grams results in higher accuracy.

The working principle is based on the diffraction of X-ray beam to different specific directions due to the crystal structure of the specimen. The x-rays are produced by bombarding a metal target, Cu for the model of XRD system used, with a beam of

electrons emitted from hot tungsten filament. X-ray diffraction occurs when the targeted atoms are ionized by the bombarded rays and emit X-ray when electrons drop from elevated energy level to lower energy levels. The angles and intensities of the diffraction, when measured, give a picture of the three-dimensional structure of the crystal.

Elastic scattering is the phenomenon where the x-ray radiation strikes the atoms' electrons and create a secondary spherical waves. According to Bragg's law, constructive interference of the waves occurs in a few specific directions, as given in Equation (3-3).

$$2 d \sin\theta = n \lambda \quad (3-3)$$

where

d = spacing between diffracting planes

θ = incident angle

n = any integer

λ = wavelength of the beam

The image produced from XRD technique has lower resolution when the crystal specimen's repeating unit cell becomes larger and more complex. Therefore, high resolution can often be obtained for small-molecule crystals (< 100 atoms in asymmetric unit).

The Rigaku Miniflex II System shown in Figure 3-6 uses $\text{CuK}\alpha$ ($\lambda=1.542 \text{ \AA}$) at 30 kV and 15 mA. The structure, crystalline phases and crystallite size of natural or synthetic materials can be obtained from the analysis. The specimen was initially ground to fine powder (< 100 μm). Then, it was placed on a glass specimen holder and pressed using a glass slide. Analysis was carried out by scanning from 3° to 80° at a speed of 1°/min. Peaks obtained from the analysis were evaluated using The International Centre for Diffraction Data (ICDD) database search match interpretation method to determine the type of phases present.



Figure 3-6: Rigaku Miniflex II.

The simple schematic diagram is shown in Figure 3-7.

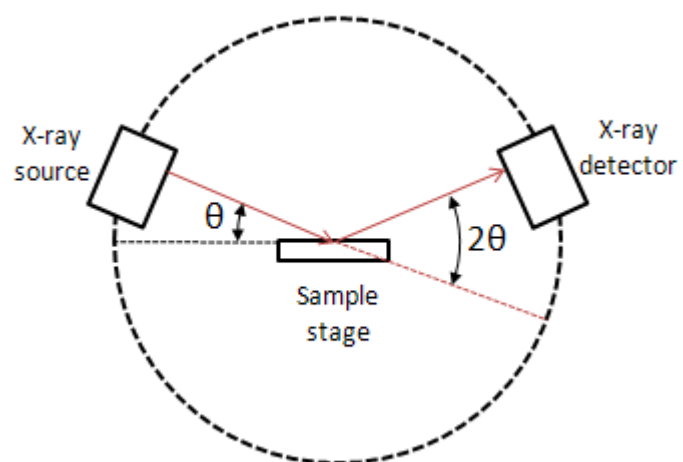


Figure 3-7: Schematic Diagram of XRD.

3.4 Preliminary Study: Methylene Blue Photocatalytic Degradation

The photocatalytic reaction was carried out in a multi-ports quartz photoreactor. It was comprised of two housings whereby a 500 mL flask with flat end was employed as methylene blue solution container whilst the smaller diameter housing, as shown in Figure 3-8, hosted a vertically-built Xenon lamp. The second smaller housing acted as protection layer to avoid direct contact between the Xe-light source and the methylene blue solution.

For the photoactivity assessment study, a total of 200 mL of 20 ppm methylene blue solution was used in each run. Reaction was carried out under atmospheric pressure and room temperature. A total of 0.2 g CuFe_2O_4 photocatalyst was added into the methylene blue solution, yielding a catalyst loading of 1.0 g L^{-1} , as illustrated in Figure 3-9. Next, the solution mixture was magnetic-stirred for 30 min to ensure homogeneity. After achieving homogeneity, the light-containing housing was locked into the reactor flask. Before reaction commenced, 7.5 mL of sample was obtained using a dropper from the port located at the side of the reactor flask, labelled R-0 (reactant at $t=0$ min). The visible light source was then switched on, and timer was started. An approximately 7.5 mL sample was obtained at the first hour and subsequently at every 30 min interval, labelled R-60, R-90, R-120, R-150 and so forth. The collected samples in centrifuge tubes were kept in a dark place to prevent further photoreaction.

The procedure was repeated with the same catalyst loading and 0.5 mL H_2O_2 , and without both catalyst and H_2O_2 as the blank. For the addition of H_2O_2 , samples were collected every 20 minutes for 2 h only because the reaction has been accelerated with the creation of Fenton system.



Figure 3-8: Xenon lamp housing of photoreactor.



Figure 3-9: Addition of catalyst into the larger diameter housing of photoreactor containing methylene blue solution.

3.5 Glycerol Photocatalytic Degradation Study

The photocatalytic reaction of glycerol was carried out with similar procedure as methylene blue as detailed in Subtopic 3.4.

For the photocatalytic degradation of glycerol study, a total of 200 mL of 0.5 v/v % glycerol solution was used in each run at ambient conditions. A total of 0.4 g CuFe_2O_4 photocatalyst was added into the glycerol solution, yielding a catalyst loading of 2.0 g L^{-1} . Different volumes of 30% hydrogen peroxide, H_2O_2 , namely 0.1 mL, 0.5 mL, 1.0 mL and 2.0 mL, were added to study the effect of H_2O_2 quantity to the photocatalytic reaction. The setup of the experiment was similar to the photodegradation of methylene blue. After obtaining the first sample, R-0, an approximately 5.0 mL sample was obtained at every 15 min interval for the first 1 h, labelled R-15, R-30, R-45 and R-60. The subsequent samples were collected at every 1 h interval until the fourth hour. The collected samples in centrifuge tubes were kept in a dark place to prevent further photoreaction.

The procedure was repeated with $\text{La-CuFe}_2\text{O}_4$, and with H_2O_2 volume of 0.5 mL and 1.0 mL.

During the reaction, the photoreactor was shield from the surrounding light as shown in Figure 3-10.



Figure 3-10: Set up during the experiment.

3.6 Sample Analysis

The samples in this study were methylene blue solution in the preliminary assessment study and glycerol solution in the core study. Samples of methylene blue solution were analysed using UV-Vis Spectrophotometer while samples of glycerol solution were analysed using high performance liquid chromatography (HPLC).

3.6.1 UV-Vis Spectrophotometer

The samples collected in centrifuge tubes were centrifuged at 10000 rpm for 10 min to separate the catalyst from the reactant samples. Subsequently, the diluted samples were carefully transferred into UV-Vis cuvettes and the surface of the cuvette was wiped with Kimwipes. Using UV-Vis model Jasco V-550 Spectrophotometer, a blank sample of distilled water was analysed and set as the baseline for the analysis, followed by the methylene blue samples.

UV-Vis spectrophotometer is commonly utilized to obtain the band-gap energy value, E_{bg} of a solution. It functions based on the principle that electrons absorb ultraviolet and visible light energy to be excited to higher anti-bonding molecular orbitals. The lower the band gap of a molecule, the more easily it can be excited, thus the longer the wavelength it absorbs. Therefore, from the wavelength absorbed by the specimen, the band-gap energy can be determined.

This quantitative method of analysis is also used to determine the concentrations of a species, where concentration is proportional to the absorbance of a particular wavelength. The wavelength absorbed is in turn used to determine the band-gap energy of the species.

The relationship between absorbance and concentration can be shown in Beer-Lambert law, as in Equation (3-4).

$$A = \log_{10}(I_0 / I) = \epsilon cL \quad (3-4)$$

where

A= measured absorbance (AU)

I_0 = intensity of the incident light at a given wavelength

I = transmitted intensity

ϵ = molar absorptivity or extinction coefficient

c = concentration of absorbing species

L = path length through the sample

The Hitachi U-1800 Spectrophotometer used in this research has a single monochromator optical system with double beam. The light is sourced from deuterium lamp for wavelength 190 to 350 nm and halogen lamp for wavelength 330 to 1100 nm, thus yielding a wavelength range from 190 to 1100 nm. The photometric display is up to four digits Abs. This model of UV-Vis spectrophotometer is shown in Figure 3-11.



Figure 3-11: Hitachi U-1800 Spectrophotometer.

Figure 3-12 shows the working mechanism of a UV-Vis spectrophotometer with deuterium lamp and tungsten lamp as the optical sources. This sample illustrates the similar mechanism adapted for Hitachi U-1800 Spectrophotometer used in this research.

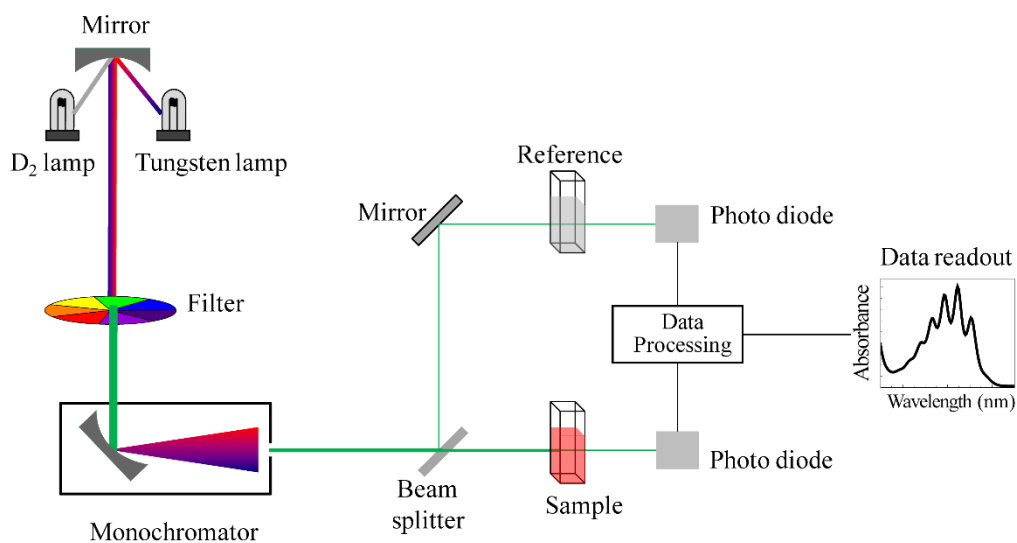


Figure 3-12: Mechanism of UV-Vis Spectrophotometer

For the sample analysis, the peak indicating methylene blue was at the range of 624 to 664 nm. The UV-Vis analysis was specified at scan speed of 200 nm/min from the starting wavelength of 800.0 nm to the ending wavelength of 500 nm. The highest peak of the spectrum, which is in direct proportion to the concentration of methylene blue solution, was determined and then recorded for each sample.

3.6.2 High Performance Liquid Chromatography (HPLC)

High performance liquid chromatography (HPLC) provides accurate and precise results of component analysis based on the chromatographic separation of different components. The solvent or mobile phase which carries the injected sample is pumped through a HPLC column packed with the stationary phase. HPLC is equipped with a detector to identify and quantify the compound according to the retention time of specific compound in the stationary phase. The detector used depends on the characteristic of the absorbance. For instance, UV-absorbance detector is used for a compound which can absorb ultraviolet light; fluorescence detector is used for a fluorescent compound; while evaporative-light-scattering detector (ELSD) is used when the compound has none of the characteristic mentioned. ELSD is a more universal type of detector applicable for all compound. (Swadesh, 2001)

The separation of compound in HPLC can be described by Equation (3-5).

$$R_s = \frac{1}{4} \left(\frac{\alpha - 1}{\alpha} \right) \sqrt{N} \quad (3-5)$$

Where R_s is the degree of resolution between two peaks in a chromatogram,
 α is the ratio of the retention factors of the two compounds
and N is the column plate number.

Significantly, larger N and α values give a better separation. A complete separation requires $RS > 1.2$. (Hanai, 1999)

The operation of HPLC is illustrated in Figure 3-13.

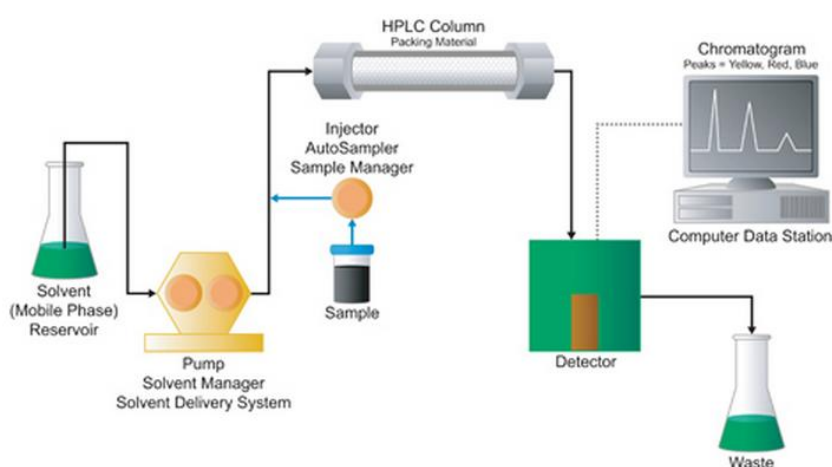


Figure 3-13: The Operating Parts of HPLC.

For the analysis of glycerol solution in this study, the column used for Agilent HPLC Series 1200 was Zorbax Carbohydrate, with dimension measured 4.6 mm, 250 mm and 5 μm . The model of HPLC and HPLC column are shown in Figure 3-14 and Figure 3-15, respectively. The method settings were temperature of 30°C and flow rate of 1.0 ml/min. 99% Acetonitrile (ACN) of HPLC grade was used as the mobile phase, prepared with an ACN:water ratio of 7:3.



Figure 3-14: Agilent HPLC Series 1200.

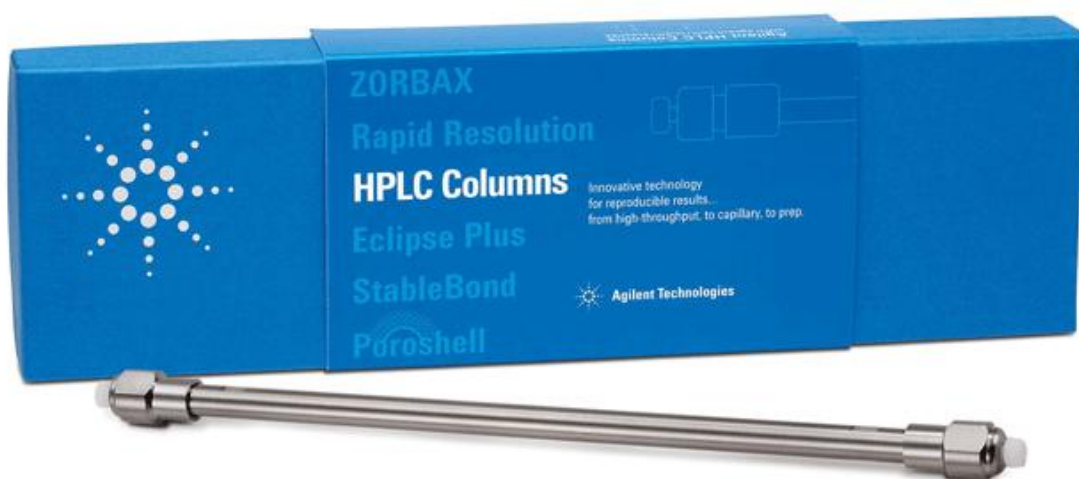


Figure 3-15: Zorbax Carbohydrate HPLC column.

3.6.2.1 Sample Preparation

The samples collected in centrifuge tubes were centrifuged at 10000 rpm for 10 min to separate the catalyst from the glycerol solution. Then, about 2 mL of each sample was carefully drawn into syringe without agitating the catalyst. The samples were filtered with 0.21 μm membrane into 1.5 mL vial. The vials filled with filtrate were labelled and collected in the sample housing for analysis.

The sample names, number and type (sample or calibration) were inserted into the computer software.

3.6.2.2 Mobile Phase Preparation

The mobile phase of the analysis was prepared by mixing ACN and ultrapure water with a ratio of 7 to 3. The mixture was then vacuum filtered and degassed with ultrasonic.

3.6.2.3 Flushing

The column was inserted to the HPLC and the mobile phase was let to flush through the system to ensure no trapped air bubbles or foreign particles and impurities from the previous operation. The column was flushed until a flat baseline was obtained. The flow rate of the mobile phase was set at 1.0 mL/min while the sample injection was pre-set at 10 μm .

3.6.2.4 Sample Analysis

By using the analysis signal of Refractive Index Signal (RID), the retention time of glycerol was shown around 3 min. After the HPLC was run, the area of the peak at the retention time of glycerol was determined from the chromatogram obtained for each sample. The area of the peak was directly proportional to the concentration of the glycerol solution.

3.6.2.5 Shut Down

After the analysis, the column was flushed with the mobile phase again to prevent the retention of any compound. The system was shut down properly after flushing.

3.7 Summary

This chapter describes the experimental procedures of this study. The preparation of CuFe_2O_4 and $\text{La-CuFe}_2\text{O}_4$ were followed by the characterization of the photocatalysts using helium displacement for gas pycnometer, N_2 physisorption BET, FESEM and XRD to determine the density, surface area, morphology and crystalline phase, respectively. Methylene blue was used as a preliminary study to assess the photoactivity of CuFe_2O_4 , followed by the core study, which was of glycerol photocatalytic degradation. Methylene blue samples were analysed using UV-Vis Spectrophotometer whereas glycerol samples were analysed using HPLC.

CHAPTER 4

4 RESULTS AND DISCUSSION

4.0 Introduction

In this chapter, physicochemical properties of the photocatalysts were characterized via several well-established techniques, namely He displacement in gas pycnometer, N₂ physisorption method, XRD and FESEM. Subsequently, photodegradation of methylene blue solution were tested as preliminary findings, followed by photodegradation of glycerol solution. Besides, this chapter also includes the correlations between photocatalytic activity and the physicochemical properties. The kinetics of the catalytic reaction over CuFe₂O₄ was also developed.

4.1 Catalyst Characterization

The characterization of catalysts in this study, *i.e.* CuFe₂O₄ and La-CuFe₂O₄, aimed to investigate the physicochemical properties of the catalysts. The characterization methods included helium displacement for gas pycnometer and N₂ physisorption for BET for the characterization of CuFe₂O₄ and La-CuFe₂O₄, as well as FESEM and XRD for the characterization of CuFe₂O₄.

4.1.1 Helium Displacement

The mass of the catalysts were weighed prior to the analysis. The mass obtained from the measurement is tabulated in Table 4-1.

Table 4-1: Mass of catalysts.

Catalyst	Mass (g)
CuFe ₂ O ₄	0.4073
La-CuFe ₂ O ₄	1.0741

Since it was set to run for 3 purges, three values of volume and thus density were obtained from the analysis. The results was presented as a Density vs Time graph. Figure 4-1 shows the result of the first set of analysis for CuFe_2O_4 , as an example of the resulting graph.

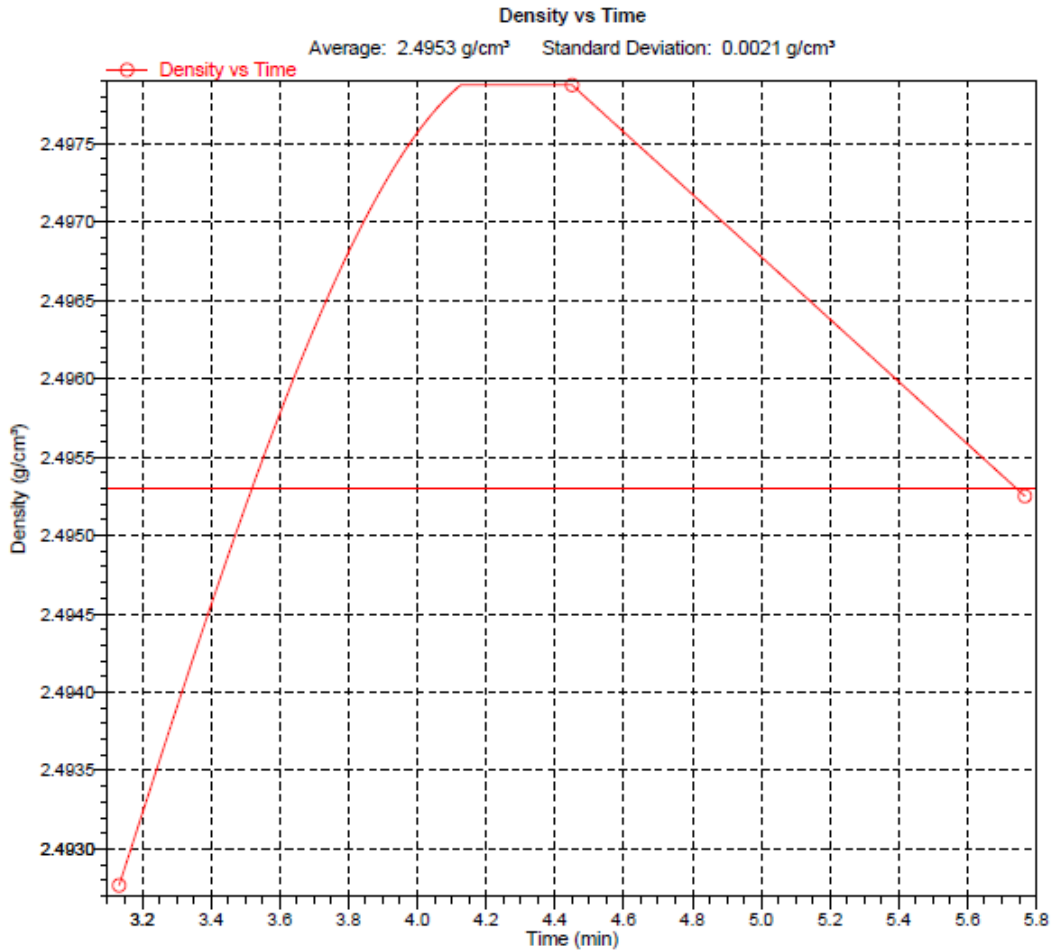


Figure 4-1: Graph of Density vs Time of copper ferrite catalyst from gas pycnometer.

The results of the analysis for CuFe_2O_4 is summarized in Table 4-2.

Table 4-2: Gas pycnometer density results of copper ferrite catalyst.

Cycle	Volume (cm ³)	Density (g/cm ³)
1	0.1634	2.4928
2	0.1631	2.4979
3	0.1632	2.4953
Average	0.1632	2.4953
Standard Deviation	0.0001	0.0021

Table 4-3 shows the analysis results for La-CuFe₂O₄.

Table 4-3: Gas pycnometer density results of copper ferrite catalyst doped with lanthanum.

Cycle	Volume (cm ³)	Density (g/cm ³)
1	0.3094	3.4714
2	0.3093	3.4730
3	0.3090	3.4757
Average	0.3092	3.4734
Standard Deviation	0.0002	0.0018

From the density analysis, it was observed that the density of La-CuFe₂O₄ was higher than the density of CuFe₂O₄. This is because the dopant, La fills the intermolecular spaces between CuFe₂O₄, and has a relatively high molar mass of 138.91.

4.1.2 Brunauer-Emmett-Teller (BET)

In the BET analysis, data of adsorbed nitrogen in term of volume (V_{ads}) and number of moles (n_{ads}) at different pressures were interpreted using various methods to obtain the analysis results regarding the surface properties of the catalysts.

The isotherm of CuFe₂O₄ is shown in Figure 4-2. Isotherms obtained from plotting as V_{ads} versus p/p^0 provides the information of pore volume. The value of the pore volume was taken at $p/p^0 = 0.95$.

The two curves in the isotherm plot were the result of the adsorption and desorption of nitrogen molecules on the CuFe₂O₄ sample. At low pressures, the nitrogen molecules began to fill the pores of the CuFe₂O₄ rapidly, thus resulting in the steep curve at the beginning. As the pressure continued to increase, the surface pores were eventually covered by nitrogen. The amount of nitrogen molecules adsorbed was therefore not so affected by the increase in pressure. This occurred in the middle phase of the isotherm. BET Isotherm applies the assumption that all sites on the sample surface are equivalent. However, deviation occurred at high pressures due to the presence of cracks and indents. These surfaces could only hold a few monolayers of nitrogen at lower pressures. High pressure forced the adsorption of nitrogen to more layers, thus the curve turned steep at the end of the Isotherm.

From Figure 4-2, it can be observed that the adsorption and desorption curve has deviated to form hysteresis loop. This hysteresis phenomena showed that the pores on the

samples was mesopores. Generally, adsorption of an equilibrium amount of adsorbate is a reversible process, resulting in a same curve for adsorption and desorption. However, in the case of curved surfaces, such as the mesoporous surface in this case, the amount of nitrogen molecules adsorbed upon increasing or decreasing the gas pressure do not coincide over a certain interval of pressures. Capillary condensation is a phenomena of liquid-gas phase transitions under porous confinement which explains the resulting hysteresis loop. According to Naumov (2009), a fluid condenses at a vapor pressure below the bulk saturated vapor pressure in a capillary. Therefore, the occurrence of hysteresis phenomena in the Isotherm curves showed that the surface of both CuFe_2O_4 and $\text{La-CuFe}_2\text{O}_4$ consisted of mesopores.

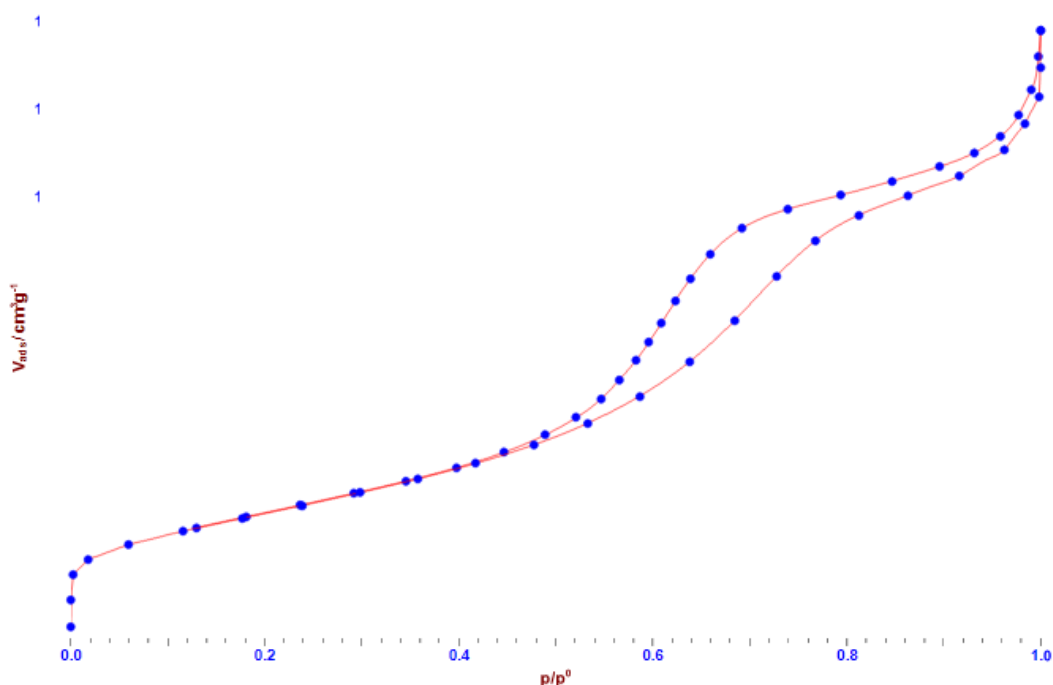


Figure 4-2: Isotherm of copper ferrite from BET analysis.

For the determination of the surface area of the catalysts, models such as Langmuir method, 2-Parameters Line and 3-Parameters Fit were employed. The graphs for the three methods were plotted as $p/(V_{\text{ads}} p^0)$ versus p/p^0 , $p/(V_{\text{ads}}(p^0-p))$ versus p/p^0 , and V_{ads} versus p/p^0 , respectively. Among the three methods, 2-Parameters Line showed the highest regression value of 0.9999, with the graph as shown in Figure 4-3.

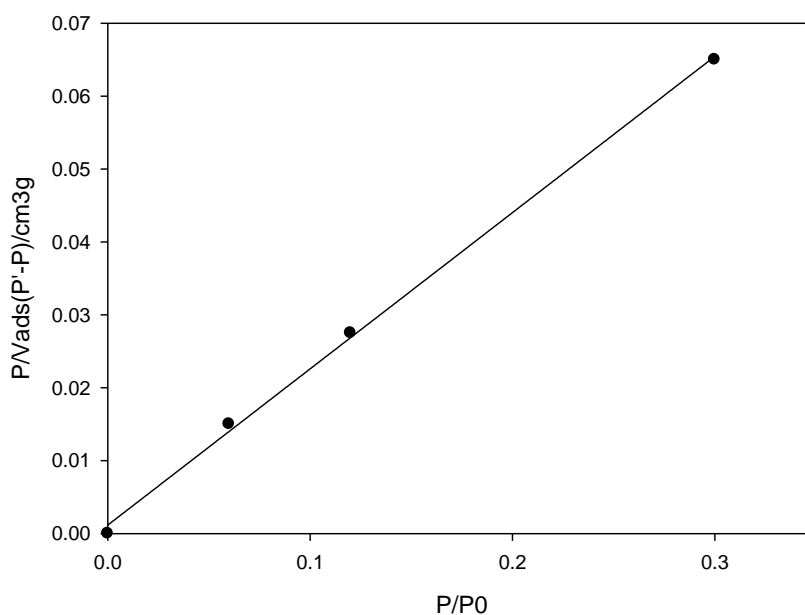


Figure 4-3: Surface area of copper ferrite by 2 Parameters Line from BET analysis.

The last parameter determined from BET analysis was the mesopores of the catalysts. The methods utilized were Barret-Joyner-Halenda (BJH), Cranston and Inkley, Modelless, and Horvath and Kawazoe. The results obtained from the BET analysis are summarized in Table 4-4.

Table 4-4: BET analysis results for copper ferrite catalyst with and without lanthanum dopant.

Characteristic	Method	Catalyst	
		CuFe ₂ O ₄	La-CuFe ₂ O ₄
Pore Volume	Isotherm	0.1683 cm ³ g ⁻¹	0.1669 cm ³ g ⁻¹
Surface Area	Langmuir	347.92 m ² g ⁻¹	173.69 m ² g ⁻¹
	BET 2-Parameters Line	102.37 m ² g ⁻¹	53.934 m ² g ⁻¹
	BET 3-Parameters Fit	100.1 m ² g ⁻¹	53.022 m ² g ⁻¹
Mesopores	BJH	136.13 m ² g ⁻¹	74.58 m ² g ⁻¹
	Cranston and Inkley	127.11 m ² g ⁻¹	67.79 m ² g ⁻¹
	Modelless	115.91 m ² g ⁻¹	78.481 m ² g ⁻¹
	Horvath and Kawazoe	100.99 m ² g ⁻¹	54.899 m ² g ⁻¹

From the analysis results, La-CuFe₂O₄ has lower pore volume, surface area and mesopores as compared to CuFe₂O₄. This is unfavourable in term of photocatalytic activity because high values of these characteristics aid the adsorption of reactants on the catalyst surface.

In surface area analysis, the Langmuir graph of both catalysts showed low regression. This explained the great difference between the surface area obtained from Langmuir and those obtained from the other two methods. Therefore, the surface area from BET 2-Parameters Line and BET 3-Parameters Fit were more accurate than the Langmuir values.

4.1.3 Field Emission Scanning Electron Microscope (FESEM)

The FESEM analysis was performed on copper ferrite photocatalyst only as it served as the backbone of the synthesized photocatalysts. FESEM images were obtained at several magnifications before calcination of the catalyst, after calcination, and after the utilization of the catalyst in photocatalysis experiment.

Figure 4-4 (a), Figure 4-4 (b) and Figure 4-4 (c) show the FESEM images of copper ferrite photocatalyst before calcination at magnification of 5000, 30000 and 50000 times, respectively. The catalyst structure was not formed yet before calcination, thus lacking a well-crystallized structure.

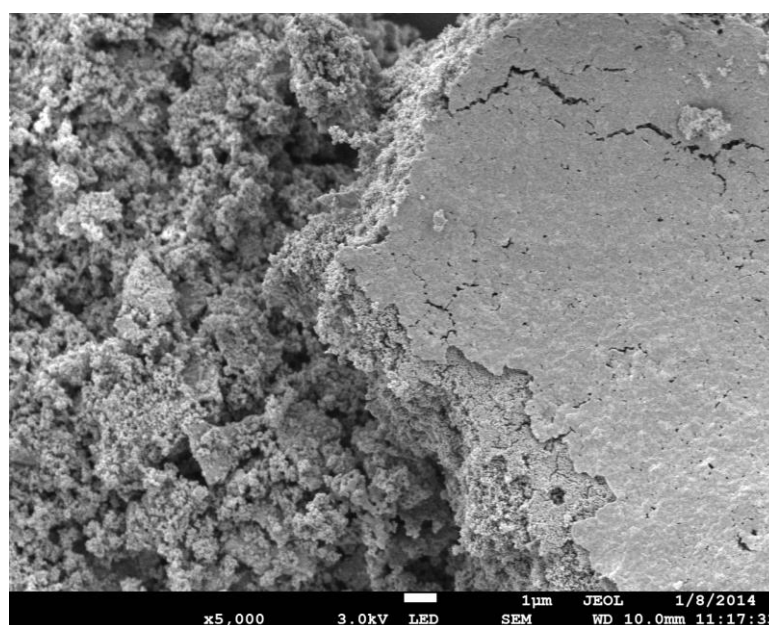


Figure 4-4 (a): FESEM image of copper ferrite before calcination at 5,000 times magnification.

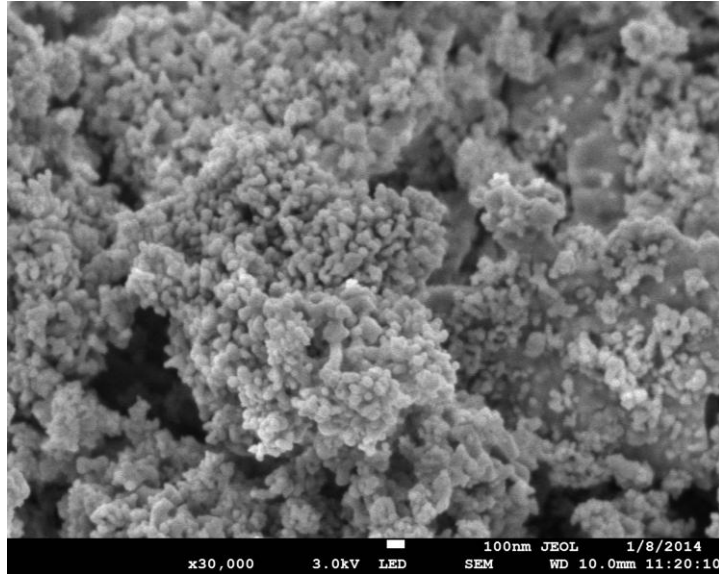


Figure 4-4 (b): FESEM image of copper ferrite before calcination at 30,000 times magnification.

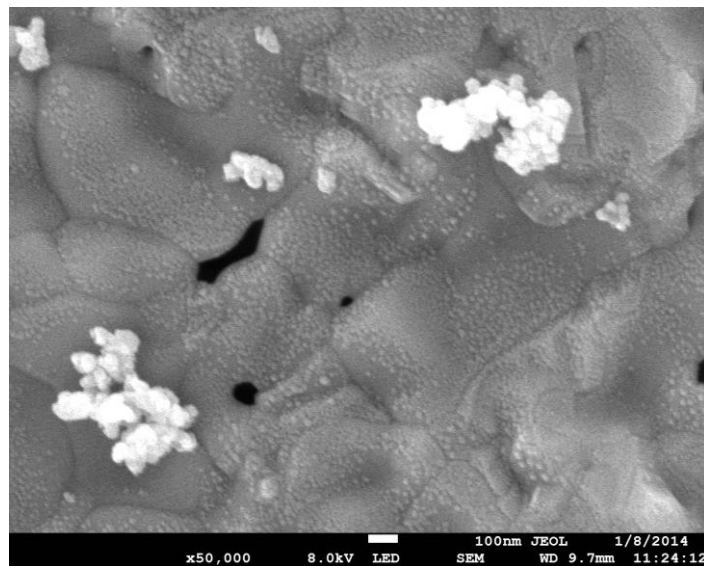


Figure 4-4 (c): FESEM image of copper ferrite before calcination at 50,000 times magnification.

Figure 4-5 (a), Figure 4-5 (b) and Figure 4-5 (c) show the FESEM images of copper ferrite after calcination at 5000, 30000 and 50000 times magnification, respectively. After calcination at 900 °C, the compound has a more significant crystalline structure.

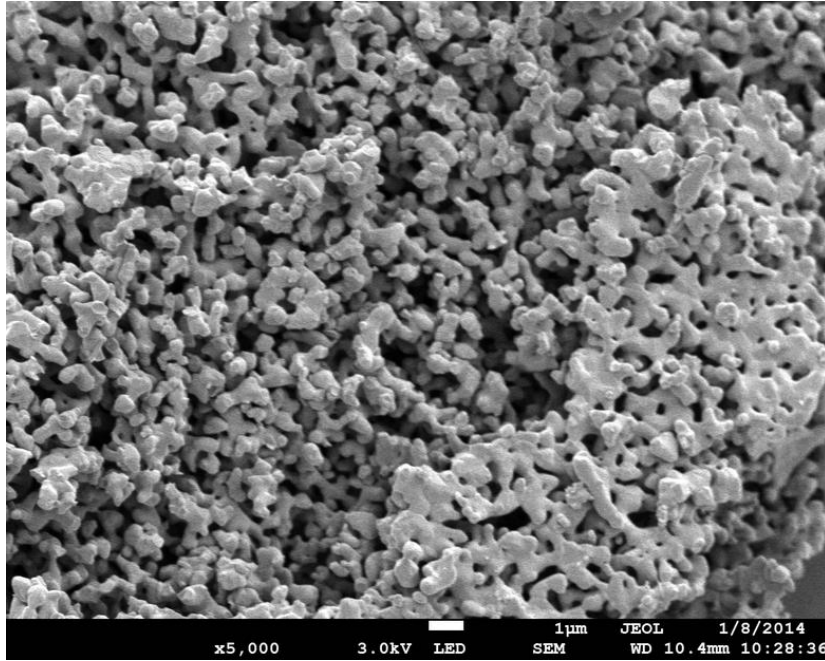


Figure 4-5 (a): FESEM image of copper ferrite after calcination at 5,000 times magnification.

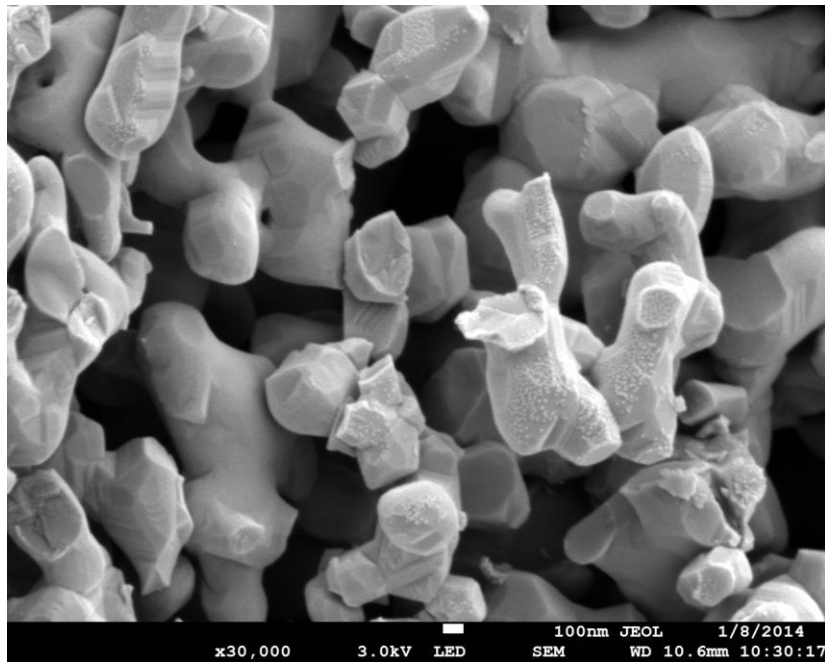


Figure 4-5 (b): FESEM image of copper ferrite after calcination at 30,000 times magnification.

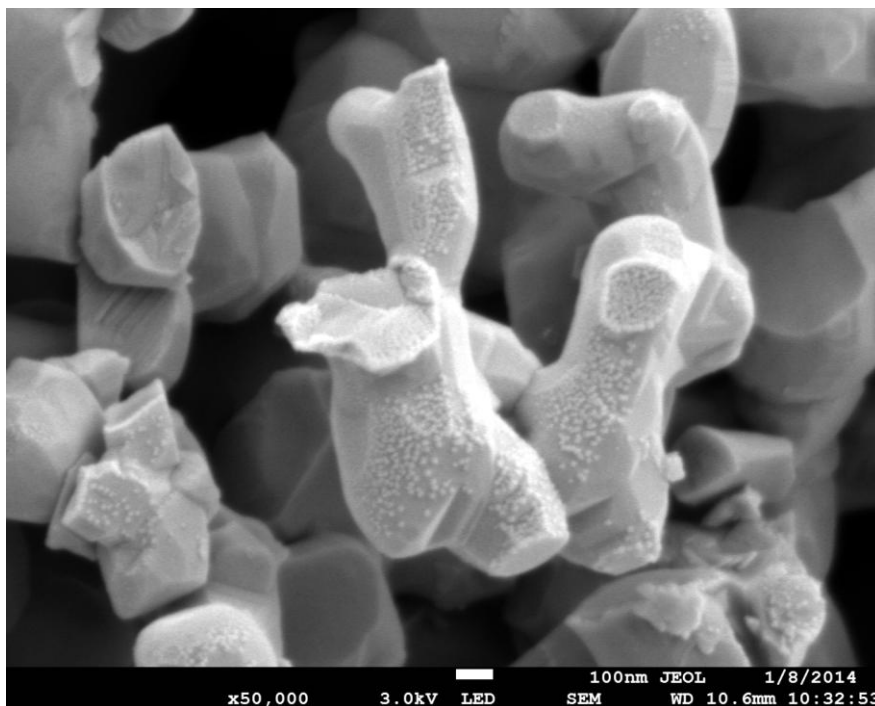


Figure 4-5 (c): FESEM image of copper ferrite after calcination at 50,000 times magnification.

Copper ferrite catalyst exhibited coral-like crystalline structure at size up to several hundred nanometers. Calcination significantly changed the morphological structure of copper ferrite and resulted in greater total surface area. Agglomerated grains with visible grain boundaries could be observed from the calcined catalyst.

4.1.4 X-Ray Diffraction (XRD)

The peaks in XRD pattern obtained from copper ferrite analysis was smoothed to obtain the pattern as shown in Figure 4-6. For the La-promoted CuFe_2O_4 , due to the equipment limitation, a similar XRD diffractogram as the one in Figure 4-6 was obtained; hence it is not presented. Each peak from the XRD pattern indicated different crystal structure and size, as denoted by the miller indices in Table 4-5. All the peaks indicated copper ferrite, CuFe_2O_4 except the peaks at $2\theta = 33.30^\circ$ and $2\theta = 38.87^\circ$, where the species is unknown. The solid sample thus may consisted of amorphous solid which had not been detected by XRD technique, possibly copper, iron oxides or copper ferrite in amorphous state (Deraz, 2010).

The peaks were indexed to the (1 0 1), (1 1 2), (1 0 3), (2 1 1), (2 0 2), (3 1 2) and (2 2 4) planes of a face-centered cubic of CuFe_2O_4 .

Deraz (2010) reported that the intensities of (2 2 0) and (4 0 0) or (4 4 0) planes are more sensitive to the cations on tetrahedral or octahedral sites, respectively. These planes, however, were absent from the analysis results obtained. Therefore, the synthesized copper ferrite did not exist in tetrahedral or octahedral structure.

The angular analysis from XRD presents angular characteristics of $\alpha = \beta = \gamma = 90^\circ$. This agrees with the face-centered cubic structure of the CuFe_2O_4 sample.

The Scherrer Equation, shown in Equation (4-1), was used to calculate the crystallite size of the catalyst as tabulated in Table 4-5 (Wang *et al.*, 2014).

$$D_{hkl} = \frac{K\lambda}{\beta_{hkl} \cos \theta_{hkl}} \quad (4-1)$$

Where D_{hkl} is the crystallite size perpendicular to the normal line of the (hkl) plane;

K is a constant, 0.89;

β_{hkl} is the full width at half maximum (fwhm) of the (hkl) diffraction peak;

θ_{hkl} is the Bragg angle of the (hkl) peak; and

λ is the X-ray wavelength.

The sizes of the crystallite range from 109 μm to 588 μm , which is consistent to the images obtained from FESEM analysis in Subtopic 4.1.3.

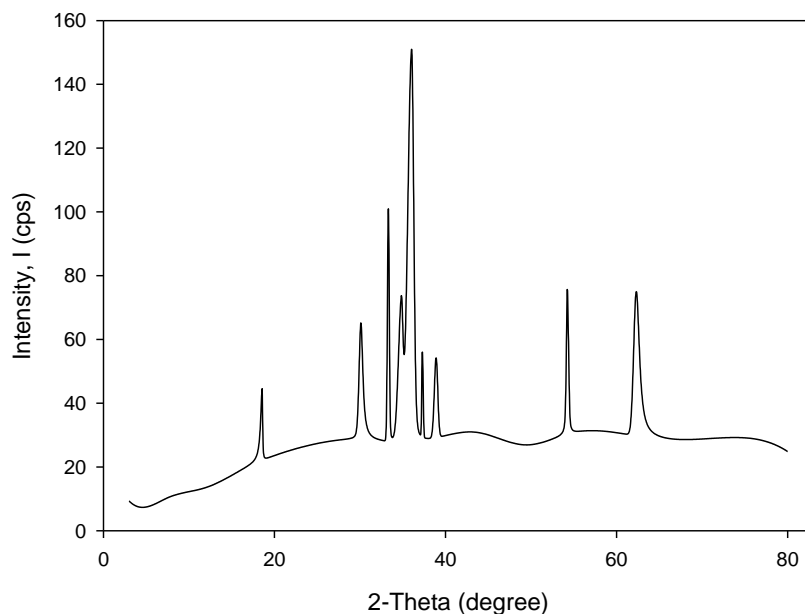


Figure 4-6: XRD pattern of copper ferrite.

Table 4-5: Analysis of peaks from XRD pattern of copper ferrite.

2-Theta (degree)	Size (μm)	Miller indices
18.56	312	(1 0 1)
30.082	170	(1 1 2)
33.30	383	Unknown
34.82	141	(1 0 3)
36.03	109	(2 1 1)
37.27	588	(2 0 2)
38.87	195	Unknown
54.23	396	(3 1 2)
62.25	129	(2 2 4)

4.2 Photocatalytic Activity Assessment with Methylene Blue Solution

The experiment was run with only one concentration of MB without varying any parameters. This is because this experiment aimed at only to assess the photocatalytic activity of the CuFe₂O₄ photocatalyst, which formed the bulk of catalyst material, and the effectiveness of Fenton system.

The concentration change was shown based on the normalized concentration, C/C_0 , where C is the concentration of the methylene blue at current time, while C_0 is the initial concentration of the methylene blue. C/C_0 is also defined as the undecomposed fraction of the methylene blue. It can be related to the conversion of methylene blue by Equation (4-2).

$$Conversion(\%) = \left(1 - \frac{C}{C_0}\right) \times 100\% \quad (4-2)$$

Figure 4-7 shows the trend of concentration changes in blank, photocatalytic run and the Fenton system run. The slight decline in concentration ratio shown by the blank run is due to photoreaction. The methylene blue degrades under the radiation of visible light itself in a very slow rate. With catalyst, the rate of degradation significantly increases, indicating photocatalytic activity. The degradation of methylene blue was further enhanced with the addition of H₂O₂ to create a photo-Fenton system.

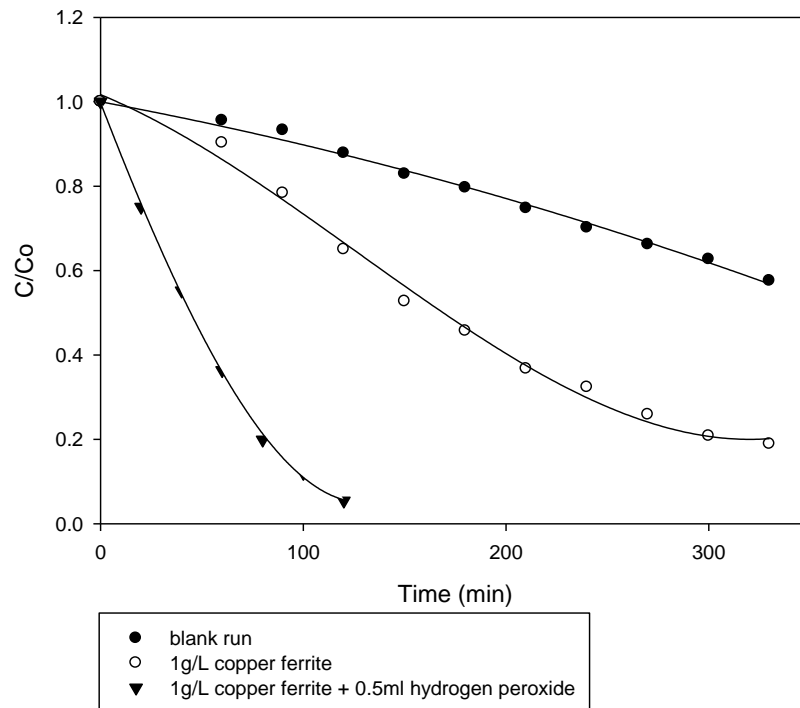


Figure 4-7: Graph of C/Co versus time for methylene blue photocatalytic degradation, photo-Fenton degradation and blank run.

Figure 4-8 depicts the decreasing colour intensity of the methylene blue solution over time due to the decreasing of methylene blue's concentration. The change in colour intensity shows obvious activity of the photocatalyst.



Figure 4-8: Phtocatalytic effect on methylene blue (increasing time from left to right).

4.3 Glycerol Photocatalytic degradation

The samples from glycerol photodegradation were analysed using HPLC technique. The results of the analysis were presented as chromatogram as shown in Figure 4-9. The peak at around 3.2 min retention time indicates the presence of glycerol in the sample, while the area under the peak proportionate to the concentration of glycerol (Bidlingmeyer, 1992). Therefore, the normalized concentration, C/C_0 is having the same value as A/A_0 , as shown in Equation (4-3).

$$\frac{C}{C_0} = \frac{A}{A_0} \quad (4-3)$$

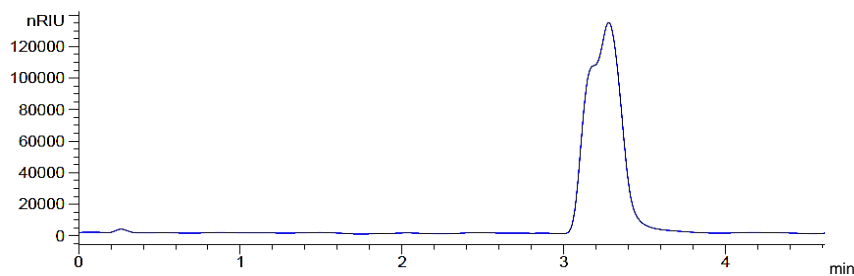


Figure 4-9: Chromatogram of glycerol at t=0 min in photodegradation over 2.0 g/L copper ferrite and 0.1ml hydrogen peroxide.

The results of glycerol degradation over 2.0 g/L CuFe_2O_4 and 2.0 g/L $\text{La-CuFe}_2\text{O}_4$ at various volume of H_2O_2 added are summarized in Table 4-6 and Table 4-7, respectively. The concentration, similar to methylene blue concentration in Subchapter 4.2, were recorded in term of C/C_0 . The relationship between glycerol conversion to C/C_0 can also be explained by Equation (4-2).

Table 4-6: Normalized concentration of glycerol (C/C_0) after 4 h degradation over 2.0 g/L copper ferrite.

Time (min)	Blank run	0 mL H₂O₂	0.1mL H₂O₂	0.5mL H₂O₂	1.0mL H₂O₂	2.0mL H₂O₂
0	1.00	1.00	1.00	1.00	1.00	1.00
15	1.00	-	0.99	-	0.98	0.93
30	1.00	-	0.98	-	0.92	1.00
45	1.00	-	1.00	-	1.00	0.91
60	1.00	1.00	1.00	1.00	0.93	0.89
120	1.00	1.00	1.00	0.97	1.00	0.96
180	1.00	1.00	1.00	0.91	0.94	0.93
240	1.00	1.00	1.00	0.91	0.92	1.00

Table 4-7: Normalized concentration of glycerol (C/C_0) after 4 h degradation over 2.0 g/L lanthanum doped copper ferrite.

Time (min)	Blank run	0.5 mL H₂O₂	1.0 mL H₂O₂
0	1.00	1.00	1.00
15	1.00	0.99	1.00
30	1.00	1.00	0.97
45	1.00	1.00	0.96
60	1.00	1.00	0.91
120	1.00	0.99	0.96
180	1.00	1.00	0.96
240	1.00	1.00	0.97

Figure 4-10 (a) and Figure 4-10 (b) were plotted for the comparison of the photodegradation over CuFe_2O_4 and $\text{La-CuFe}_2\text{O}_4$ at different H_2O_2 loadings. From Figure 4-10 (a), it can be observed that the extent of photodegradation increased with the increase of H_2O_2 loadings. Without H_2O_2 , the glycerol solution showed insignificant degradation after 4 h. This is most likely to be explained by the increasing amount of hydroxyl free radicals (from H_2O_2) present to catalyse the reaction. For the photocatalytic degradation over $\text{La-CuFe}_2\text{O}_4$ as shown in Figure 4-10 (b), no photodegradation was observed for 0.5 mL of H_2O_2 loading. The photodegradation was only noticeable when 1.0 mL H_2O_2 was added into the reaction. $\text{La-CuFe}_2\text{O}_4$ was thus showing weaker photocatalytic properties as compared to pure CuFe_2O_4 . The higher surface area, pore volume and mesopores of pure CuFe_2O_4 as characterized by N_2 physisorption analysis may have provide greater adsorption of the reactants to form oxidative free radicals. The photodegradation of glycerol solution over the catalyst with and without La dopant were compared at 1.0 mL

H_2O_2 loading in Figure 4-10 (c). Obviously, $CuFe_2O_4$ exhibited a higher photo-catalytic activity in the degradation of glycerol solution as compared to $La-CuFe_2O_4$.

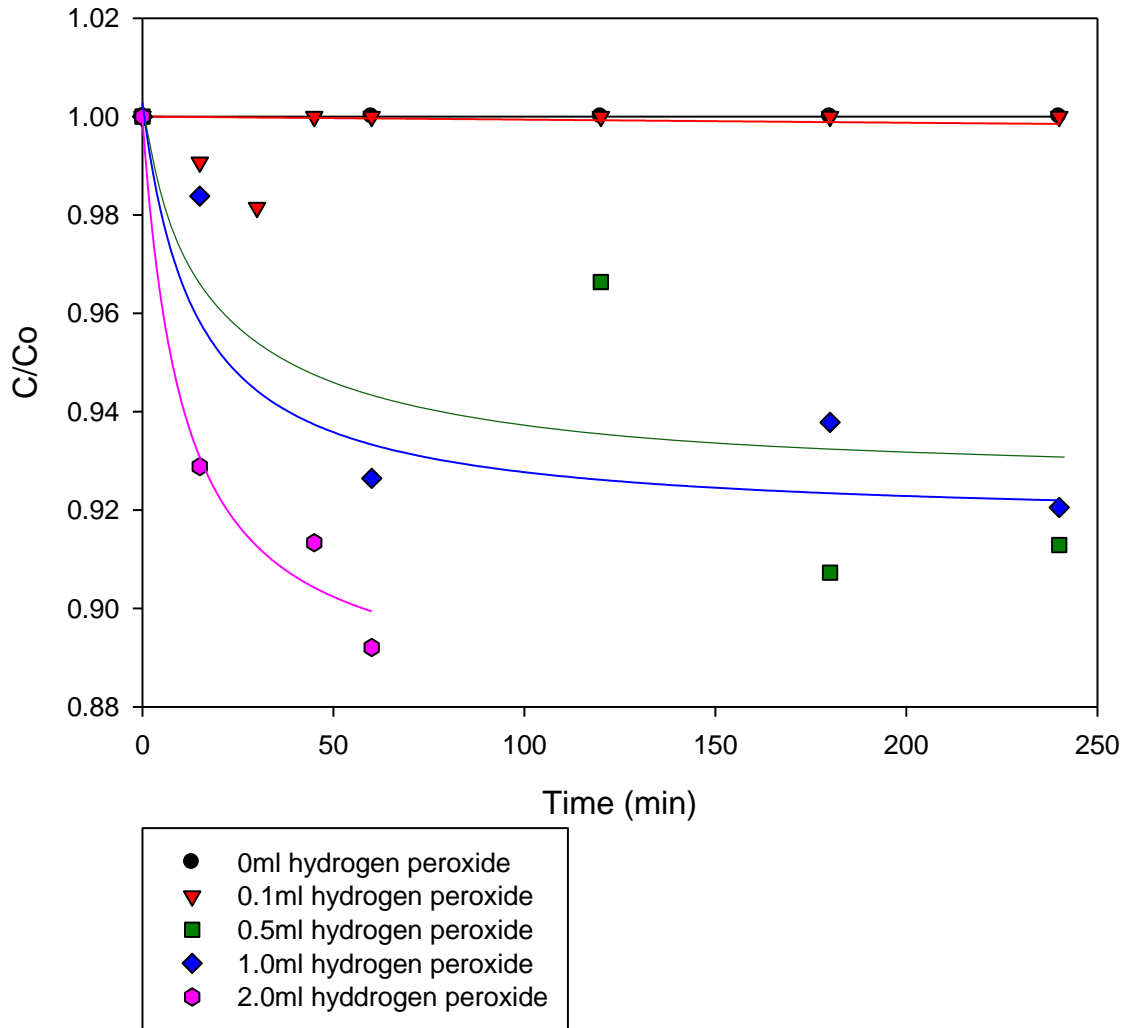


Figure 4-10 (a): Normalized concentration of glycerol for photodegradation over 2.0 g/L copper ferrite with various hydrogen peroxide loadings.

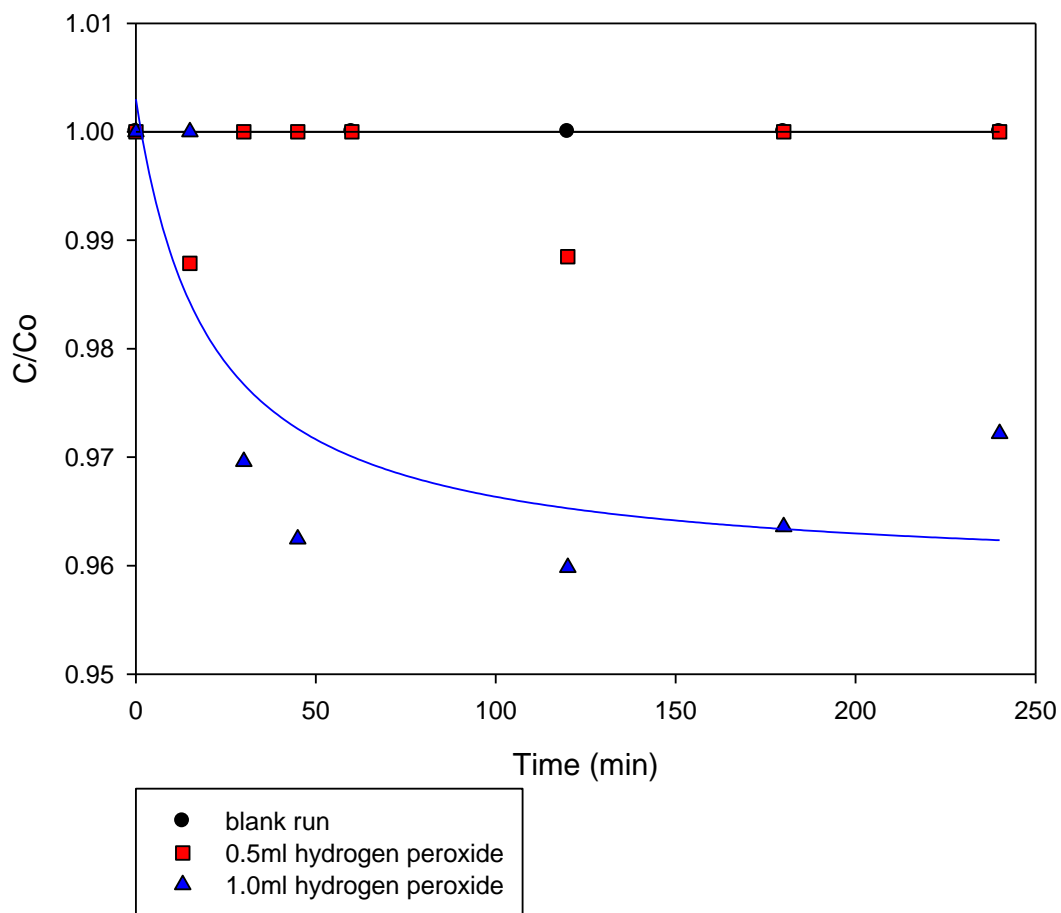


Figure 4-10 (b): Normalized concentration of glycerol for photodegradation over lanthanum doped copper ferrite with various hydrogen peroxide loadings.

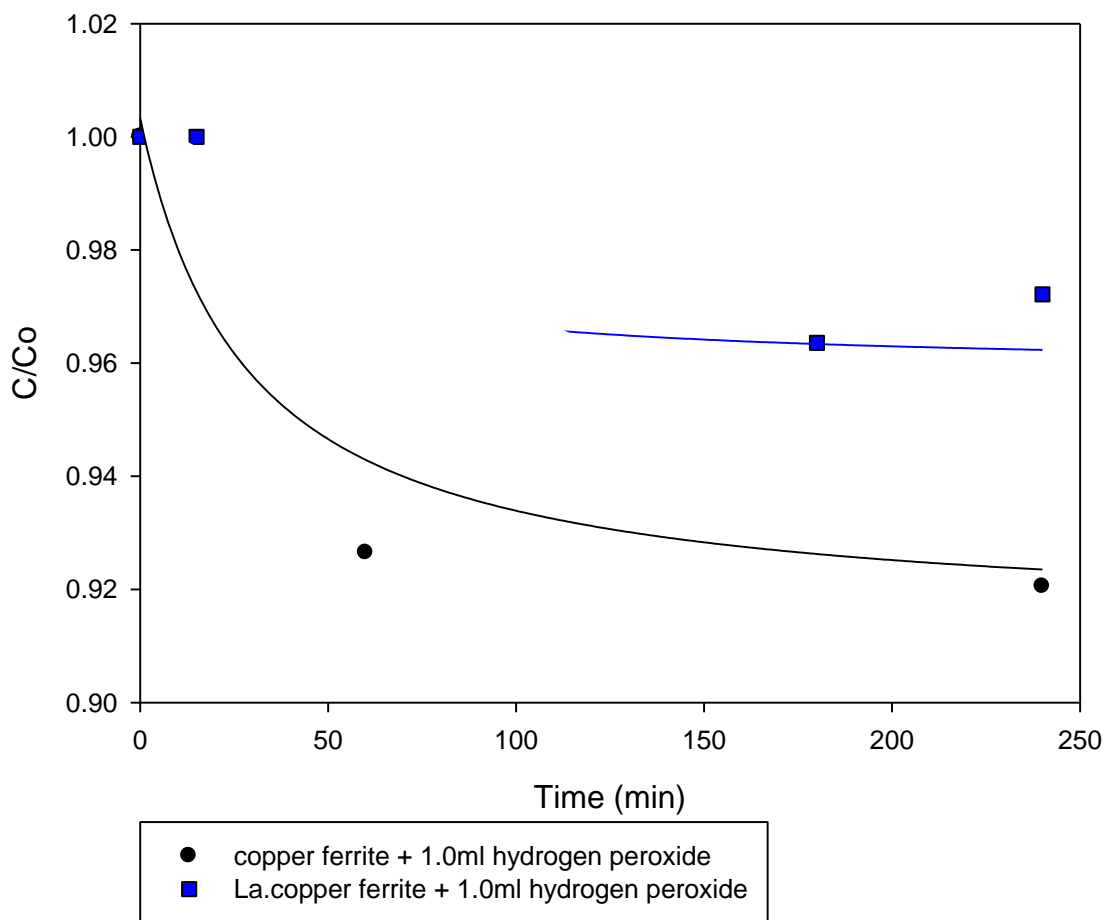


Figure 4-10 (c): Comparison of photocatalytic activity of copper ferrite with and without lanthanum dopant with 1.0 mL H₂O₂.

As compared to the photocatalytic degradation of methylene blue solution in Subchapter 4.2, CuFe₂O₄ showed significantly lower catalytic activity in the degradation of glycerol. The difference in the photocatalytic activity was possibly due to the different potential difference displayed between the reactant and the catalyst. The greater the potential difference, the more efficient the photocatalytic activity is estimated to be.

Significantly, CuFe₂O₄ exhibited a higher catalytic activity than La-CuFe₂O₄ in the photodegradation of glycerol due to the larger pore volume and surface area possessed. The photocatalytic activity increases with increasing quantity of H₂O₂ added to create a photo-Fenton system. Photodegradation of glycerol over CuFe₂O₄ occurred at a lower rate than the photodegradation of methylene blue over the same photocatalyst due to the assumption suggested.

4.4 Kinetics of Glycerol Photodegradation over Copper Ferrite

The reaction order of the photodegradation over CuFe_2O_4 can be determined using the integral method. This method requires trial and error. The differential equation of the reaction rate with the assumed reaction order was integrated and arranged to obtain a linear plot. Should the assumed reaction order was correct, the plot would be a linear plot with the obtained parameters (Fogler, 2006).

For zero order reaction, the differential equation is expressed as Equation (4-4).

$$\frac{dC_A}{dt} = -k \quad (4-4)$$

After integration, it can be rearranged to linear form as Equation (4-5). If the reaction is a zero order reaction, then the plot of C_A/C_{A0} against time (t) is a straight line with gradient of $-k/C_{A0}$ and y-intercept of unity.

$$\frac{C_A}{C_{A0}} = -\frac{k}{C_{A0}}t + 1 \quad (4-5)$$

First order differential equation is shown in Equation (4-6), and then is arranged into linear form as shown in Equation (4-7).

$$\frac{dC_A}{dt} = -kC_A \quad (4-6)$$

$$\ln \frac{C_{A0}}{C_A} = kt \quad (4-7)$$

For second order reactions, the differential equation and linear equation are shown in Equation (4-8) and Equation (4-9), respectively.

$$\frac{dC_A}{dt} = -kC_A^2 \quad (4-8)$$

$$\frac{C_{A0}}{C_A} = C_{A0}kt + 1 \quad (4-9)$$

Table 4-8 shows the values utilized to study the reaction kinetics as selected from the photodegradation of glycerol over CuFe_2O_4 and 0.5 mL of H_2O_2 . This set of experiment was extended to 5 h to provide more data for kinetics study.

Table 4-8: Values utilized to develop the kinetics of glycerol photodegradation over copper ferrite.

Time, t (h)	C_A/C_{A0}	$\ln (C_{A0}/C_A)$	C_{A0}/C_A
0	1.0000	0.0000	1.0000
1	1.0000	0.0000	1.0000
2	0.9664	0.0342	1.0348
3	0.9073	0.0973	1.1022
4	0.9129	0.0911	1.0954
5	0.8352	0.1801	1.1973

Firstly, the reaction was assumed as zero order reaction. The linear equation of the zero order reaction as shown in Equation (4-5) was plotted as demonstrated in Figure 4-11. From the plot, the R^2 value obtained was 0.8745. The slope of the graph was -0.0276. With the initial concentration of 0.5 v/v % glycerol, the reaction constant k can be calculated as $0.138 \text{ v/v \% h}^{-1}$.

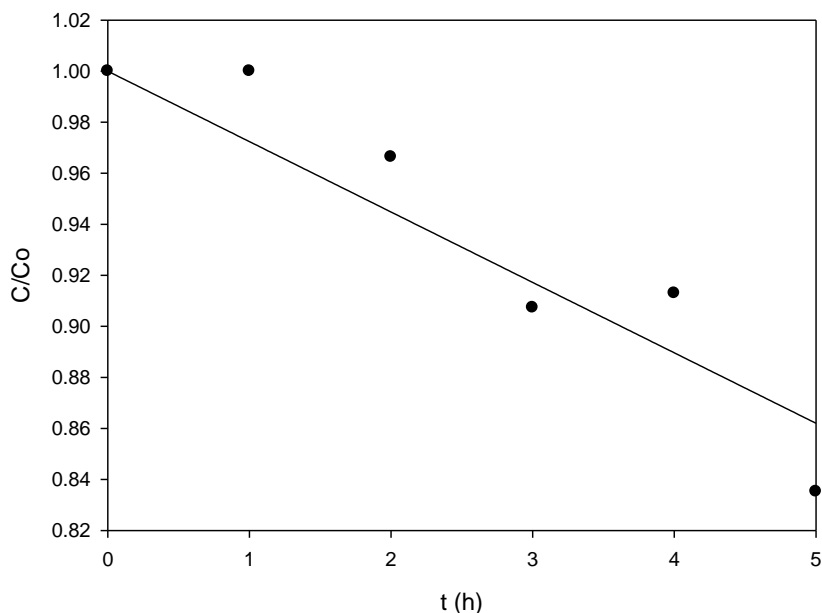


Figure 4-11: Zero order linear plot of glycerol photodegradation over copper ferrite catalyst.

Secondly, first order linear equation in Equation (4-7) was plotted as shown in Figure 4-12. The resulted R^2 value from the plot was 0.8623 whereas the value of the slope was 0.0298. From the linear equation, reaction constant k can obviously be obtained from the slope of the graph. Therefore, the k value of the first order reaction was 0.0298 h^{-1} .

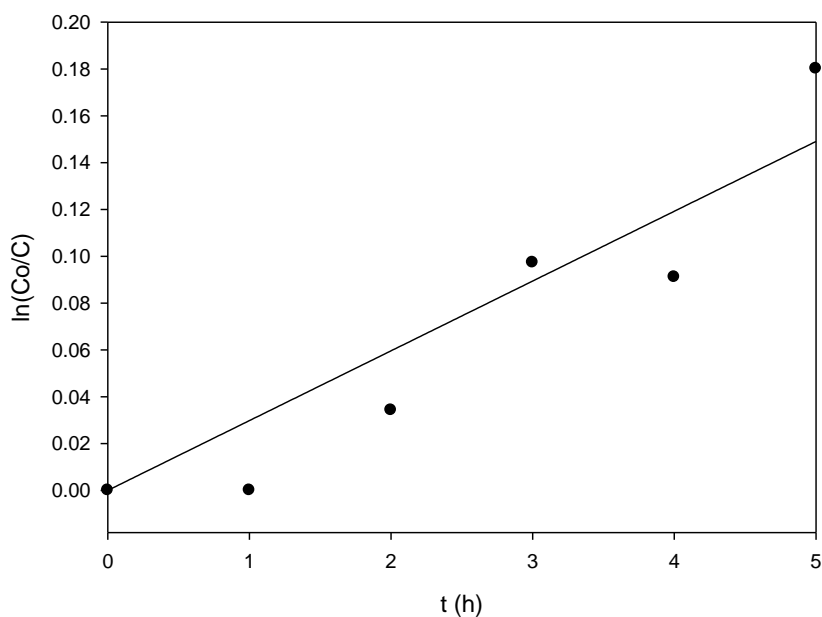


Figure 4-12: First order plot of glycerol photodegradation over copper ferrite catalyst.

Finally, the linear equation of second order reaction system was plotted as illustrated in Figure 4-13. The plot of this equation gave the lowest R^2 value of 0.8489. With the slope value of 0.0317, k value was determined to be $0.0634 \text{ h (v/v \%)}^{-1}$.

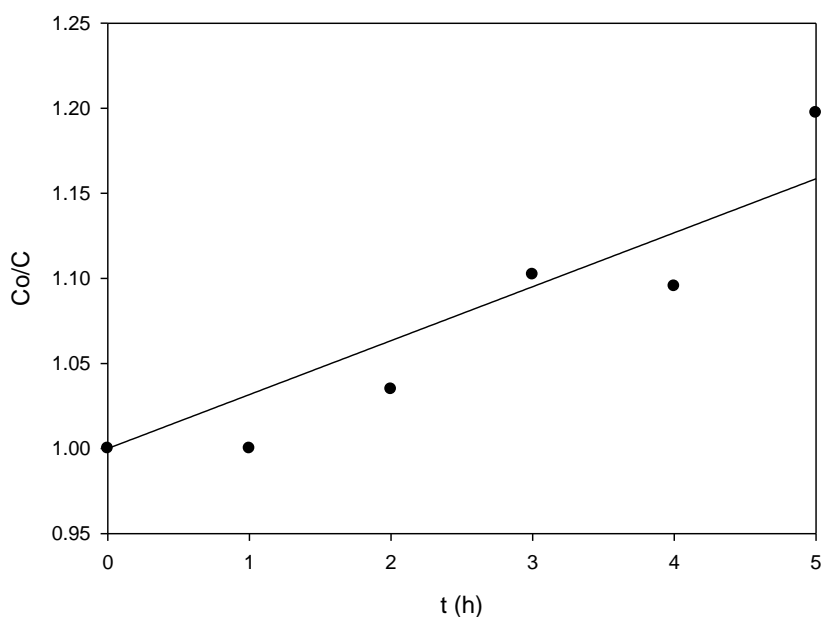


Figure 4-13: Second order plot of glycerol photodegradation over copper ferrite catalyst.

From the R^2 values, the most appropriate plot to represent the photodegradation reaction of glycerol over copper ferrite catalyst was the plot of zero order linear equation as determined from the highest R^2 value of 0.8745. Therefore, the reaction can be referred to as a pseudo-zero order reaction.

In zero order reactions, the rate of reaction is independent on the concentration of reactants. Zero order reaction is common in heterogeneous catalytic reactions, such as the decomposition of nitrous oxide and the reverse Haber process. The general contribution to zero-order reaction is the small fraction of reactant molecules in the reaction pool. The low concentration of glycerol in the study matched this condition. The reaction can therefore be reasonably concluded as a pseudo-zero order reaction.

Obviously, a zero order reaction cannot continue after the reaction has been exhausted. Therefore, such reaction will revert to another rate law upon reaching a point of concentration. (Petrucci *et al.*, 2007)

The findings in this study showed that the photodegradation of glycerol over copper ferrite catalyst is a pseudo-zero order reaction with reaction constant of $0.138 \text{ v/v } \% \text{ h}^{-1}$.

CHAPTER 5

5 CONCLUSIONS AND RECOMMENDATIONS

5.1 Conclusions

The objective to synthesize and characterize CuFe_2O_4 and $\text{La-CuFe}_2\text{O}_4$, and to study the photodegradation of glycerol was achieved. The conclusions are drawn based on the scopes of study outlined in Chapter 1. The conclusions are arranged in point form to ensure consistency with the scopes.

- The photocatalysts CuFe_2O_4 (30 wt % Cu) and $\text{La-CuFe}_2\text{O}_4$ (40 wt % La) was successfully synthesized with co-precipitation method.
- The characterization of CuFe_2O_4 was done with gas pycnometer, BET, FESEM and XRD, whereas the characterization of $\text{La-CuFe}_2\text{O}_4$ was done with gas pycnometer and BET. Results from the gas pycnometer revealed that the particle density of CuFe_2O_4 was 2.4953 g/cm^3 while $\text{La-CuFe}_2\text{O}_4$ had a higher particle density of 3.4734 g/cm^3 . N_2 physisorption analysis of BET showed that CuFe_2O_4 had higher total pore volume, surface area and mesopores than $\text{La-CuFe}_2\text{O}_4$. The total pore volume obtained from Isotherm curve was $0.1683 \text{ cm}^3/\text{g}$ for CuFe_2O_4 and $0.1669 \text{ cm}^3/\text{g}$ for $\text{La-CuFe}_2\text{O}_4$. The surface area from BET 2 Parameters Line was $102.37 \text{ m}^2/\text{g}$ for CuFe_2O_4 and $53.934 \text{ m}^2/\text{g}$ for $\text{La-CuFe}_2\text{O}_4$. Lastly, BJH method gave the mesopores results of $136.13 \text{ m}^2/\text{g}$ for CuFe_2O_4 and $74.58 \text{ m}^2/\text{g}$ for $\text{La-CuFe}_2\text{O}_4$. FESEM images were obtain to determine the surface structure of CuFe_2O_4 catalyst. The catalyst showed significant coral-shaped crystallite structures at sizes slightly more than a $100 \text{ }\mu\text{m}$ to several hundred nanometers. This size was consistent with the result of XRD, where it ranged from $109 \text{ }\mu\text{m}$ to $588 \text{ }\mu\text{m}$. The crystals of CuFe_2O_4 existed in face-centered cubic structures.
- The photodegradation of 0.5 v/v % glycerol over CuFe_2O_4 was increasing with increasing quantity of H_2O_2 added. The addition of 1.0ml H_2O_2 resulted in 8% of the glycerol solution. The photocatalytic activity of CuFe_2O_4 in the degradation of glycerol was significantly lower than that in the degradation of methylene blue. For the photocatalytic reaction over $\text{La-CuFe}_2\text{O}_4$, the glycerol was degraded to a

lesser extent as compared to CuFe_2O_4 . Addition of 0.5 mL H_2O_2 showed no significant photodegradation of glycerol, whereas addition of 1.0ml H_2O_2 degraded almost 6% of the glycerol. By comparing the photocatalytic activity of CuFe_2O_4 and $\text{La-CuFe}_2\text{O}_4$, CuFe_2O_4 exhibited higher photocatalytic properties. This is due to the greater pore volume, surface area and mesopores as characterized by BET analysis.

The kinetics of the photoreaction was developed using the integral method. The photodegradation of glycerol over CuFe_2O_4 occurred as pseudo-zero order reaction with k value of $0.138 \text{ v/v \% h}^{-1}$.

5.2 Recommendations

Recommendations to improve the current work in this research project is based on the findings and observations of the study. There are recommendations suggested for future works:

- i. Improved photocatalyst preparation methods such as sol-gel method, solid-state dispersion method (SSD) and mixing annealing method could be studied to improve the photocatalytic activity of the photocatalysts. Calcination temperature and period could also be a parameter to affect the photocatalytic activity.
- ii. The photocatalysts should be sieved to maintain the consistency and minimum particle size after calcination. Small particle size provides larger total exposed surface area and this is an important parameter to affect the photocatalytic activity.
- iii. The intensity of the light should be measured before each run of the experiment to ensure consistency of this factor. Light intensity may affect the results greatly.
- iv. The operating temperature has to be maintained at a small range of deviation or constant temperature (room temperature or around 25°C) throughout the experiment. The Xenon light emits high amount of heat energy that the rate of heat removed by the water cooler system is lower than the rate of heat absorbed.
- v. HPLC test should be carried out for a few times for each samples, to prevent random errors and equipment errors, such as incomplete flushing. The filtration and transfer of sample to HPLC vial should be repeated to avoid errors caused by contamination during the process.

REFERENCES

- Abazari, R. S. (2014). A unique and facile preparation of lanthanum ferrite nanoparticles in emulsion nanoreactors: morphology, structure, and efficient photocatalysis. *Material Science in Semiconductor Processing, vol 1*, 1-6.
- Anand, P. S. (2012). A comparative study of solvent-assisted pretreatment of biodiesel derived crude glycerol on growth and 1,3-propanediol production from *Citrobacter freundii*. *Nat. Biotechnol., vol 29*, 199--205.
- Ang, G. T. (2014). Recent development and economic analysis of glycerolfree processes via supercritical fluid transesterification for biodiesel production. *Renewable and Sustainable Energy Reviews, vol 31*, 61-70.
- Bidlingmeyer, B. (1992). *Practical HPLC Methodology and Applications*. Canada: John Wiley & Sons, Inc.
- (2008). *Biodiesel 2020: A Global Market Survey, 2nd Edition*. Houston: Emerging Markets Online.
- Board, E. B. (2004). *Biodiesel Production Statistics*.
- Brown, W. F. (2012). *Organic Chemistry*. United States of America: Books/cole, Cengage Learning.
- Casbeer, E. S. (2012). Synthesis and photocatalytic activity of ferrites under visible light: A review. *Separation and purification technology, vol 87*, 1-14.
- Cheng, P. D. (2007). Visible-light responsive zinc ferrite doped titania photocatalyst for methyl orange degradation. *J. Mater. Sci., vol 42*, 9239-9244.
- Deraz, N. (2010). Size and crystallinity-dependent magnetic properties of copper ferrite nano-particles. *Journal of Alloys and Compounds, vol.501*, 317-325.
- Ding, X. A. (2014). A dual-cell wastewater treatment system with combining anodic visible light driven photoelectro-catalytic oxidation and cathodic electro-Fenton oxidation. *Separation and Purification Technology, vol 125*, 103-110.
- Dompok, B. (2010). *the use of palm biodiesel by Sime Daarby vehicles, Speech by Y.B. Tan Sri Bernard Giluk Dompok, Minister of Plantation Industries and Commodities*. Selangor.
- Fogler, H. (2006). *Elements of Chemical Reaction Engineering*. Massachusetts: Pearson Education, Inc.

- Fu, Y. C. (2012). combination of cobalt ferrite and graphene: High-performance and recyclable visible-light photocatalysis. *Applied Catalysis B: Environmental*, vol 111-112, 280-287.
- Fukuchi, S. N. (2014). Effects of reducing agents on the degradation of 2,4,6-tribromophenol in a heterogeneous Fenton-like system with an iron-loaded natural zeolite. *Applied Catalysis B: Environmental*, vol. 147, 411-419.
- Guan, Y. M. (2013). Efficient degradation of atrazine by magnetic porous copper ferrite catalyzed peroxymonosulphate oxidation via the formation of hydroxyl and sulfate radicals. *Water Research*, vol 47, 5431-5438.
- Haas, M. M. (2006). a process model to estimate biodiesel production costs. *Bioresource Technology*, vol 97, 671-678.
- Hanai, T. (1999). *HPLC: A Practical Guide*. Cambridge: The Royal Society of Chemistry.
- Hashimoto, K. I. (2005). TiO₂ Photocatalysis: A historical overview and future prospects. *Japanese Journal of Applied Physics*, vol 87, 8269-8285.
- Hidawati, E. &. (2011). Treatment of glycerin ptch from biodiesel production. *International Journal of Chemical and Environmental Engineering*, vol 5, 309-314.
- Hsieh, C. F. (2009). adsorption and visible-light-derived photocatalytic kinetics of organic dye on co-doped titania nanotubes prepared by hydrothermal synthesis. *sep. purif. thecnol.*, vol 67, 312-318.
- Johnson, D. T. (2009). The glycerin glut: options for the value-added conversion of crude glycerol resulting from biodiesel production. *Environ. Prog.*, vol 26, 338-348.
- Kato, H. A. (2003). highly efficient water splitting into H₂ and O₂ over lanthanum-doped NaTaO₃ photocatalysts with high crystallinity and surface nanostructure. *J. Am. Chem. Soc.*, vol 125, 3082-3089.
- Lee, H. L. (2014). Degradation of diclofenac and carbamazepine by the copper (II)-catalyzed dark and photo-assisted Fenton-like systems. *Chemical Engineering Journal*, v. 245, 258-264.
- Li, D. C. (2008). a new route for degradation of volatile organic compounds under visible light, using the ifunctional photocatalyst Pt/TiO₂-xN_x in H₂-O₂ atmosphere. *Environ. Sci. Technol.*, vol 42, 2130-2135.

- Luo, S. X. (2011). simultaneous detoxification of hexavalent chromium and acid orange 7 by a novel Au/TiO₂ heterojunction composite nanotube arrays. *Sep. Purif. Technol.*, vol 79, 85-91.
- Lv, H. M. (2010). Synthesis of floriated ZnFe₂O₄ with porous nanorod structures and its photocatalytic hydrogen production under visible light. *Journal of Materials Chemistry*, vol 20, 3665-3672.
- Mahmoodi, N. (2011). Photocatalytic ozonation of dyes using copper ferrite nanoparticle prepared by co-precipitation method. *Desalination*, vol 279, 332-337.
- Masahiro, M. M. (2004). Photocatalytic activity of SrTiO₃ Codoped with nitrogen and lanthanum under visiblelight illumination. *Langmuir*, vol 20, 232-236.
- McCoy, M. (2005). An unlikely impact. *Chem. Eng. News* 83, vol 8 , 19.
- Naumov, S. (2009). *Hysteresis Phenomena in Mesoporous Materials*. United States: Universitat Leipzig.
- Nichele, V. S. (2014). Hydrogen production by ethanol steam reforming: Effect of the synthesis parameters on the activity of Ni/TiO₂ catalysts. *International Journal of Hydrogen Energy*, vol 39, 4252-4258.
- Nowotny, J. B. (2014). Sustainable Practices: Solar hydrogen fuel and education program on sustainable energy systems. *International Journal of Hydrogen Energy*, vol 39, 4151-4157.
- Pagliari, M. R. (2008). Glycerol: properties and production. The future of glycerol: new usage for a versatile raw material. *Royal Society of Chemistry*, 2nd ed., 1-28.
- Panagiotopoulou, P. K. (2013). Kinetics and mechanism of glycerol photo-oxidation and photo-reforming reactions in aqueous TiO₂ and Pt/TiO₂ suspensions. *Catalysis Today*, vol 209, 91-98.
- Petrucci, R. H. (2007). *General Chemistry: Principles & Modern Applications*. Upper Saddle River: Pearson Education.
- Pott, R. H. (2013). Photofermentation of crude glycerol from biodiesel using Rhodopseudomonas palustris: comparison with organic acids and the identification of inhibitory compounds. *Bioresour. Technol.*, vol 130, 725-730.
- Pott, R. H. (2014). The Purification of crude glycerol derived from biodiesel manufacture and its use as a substrate by Rhodopseudomonas palustris to produce hydrogen. *Bioresource Technology*, vol 152, 464-470.


- Rocha, E. F.-R. (2014). Lique-liquid equilibria for ternary systems containing ethylic palm oil biodiesel + ethanol + glycerol/water: Experimental data at 298.15 and 323.15K and thermodynamic modeling. *Fuel*, vol 128, 356-385.
- Sabourin-Provost, G. H. (2009). High yield conversion of a crude glycerol fraction from biodiesel production to hydrogen by photofermentation. *Bioresour. Technol.*, vol 100, 3515-3517.
- Senthilnathan, M. H. (2010). visible light responsive ruthenium-doped titanium dioxide for the removal of metsulfuron-methyl herbicide in aqueous phase. *Sep. Purif. Technol.*, vol 75, 415-419.
- Sims, B. (2011). *Clearing the way for byproduct quality: Why quality for glycerin is just as important for biodiesel.*
- Swadesh, J. (2001). *HPLC: Practical and Industrial Applications* (2nd ed.). Florida: CRC Press.
- Tamimi, M. Q.-I. (2008). Methomyl degradation in aqueous solutions by Fenton's reagent and the photo-Fenton system. *Separation and Purification Technology*, vol. 61, 103-108.
- Teipel, U. (2005). *Energetic Materials: Particle Processing and Characterization.* Federal Republic of Germany: John Wiley & Sons.
- Tran, N. &. (2013). Conversion of glycerol to hydrogen rich gas. *Chemical Society Reviews*, vol 42, 9454-9479.
- Uddin, M. K. (2014). Synthesis, characterization and activity evaluation of visible light responsive CuFe₂O₄ catalyst. *8th MUCET 2014*. Melaka.
- Wang, Y. Z. (2014). magnetic ordered mesoporous copper ferrite as a heterogeneous Fenton catalyst for the degradation of imidacloprid. *Applied Catalysis B: Environmental*, 534-545.
- Wang, Y. Z. (2014). Magnetic ordered mesoporous copper ferrite as a heterogeneous Fenton catalyst for the degradation of imidacloprid. *Applied Catalysis B: Environmental*, vol.147, 534-545.
- Wei, H. W. (2004). preparation and photocatalysis of TiO₂ nanoparticles co-doped with nitrogen and lanthanum. *journal of materials science*, vol 39, 1305-1308.
- Xu, S. S. (2007). Preparations and photocatalytic degradation of methyl orange in water on magnetically separable Bi₁₂TiO₂₀ supported on nickel ferrite. *Sci. Technol. Adv. Mater.*, vol 8, 40-46.

- Yang, Y. J. (2007). Influences of sintering atmosphere on the formation and photocatalytic property of BaFe₂O₄. *Mater. Chem. Phys.*, vol 105, 154-156.
- Zhang, G. X. (2009). Preparation and characterization of multi-functional CoFe₂O₄-ZnO nanocomposites. *J. Magn. Mater.*, vol 321, 1424-1427.
- Zielinska, A., Kowalska, E., Sobczak, J.W., Lacka, I., Gazda, M., Ohtani, B., Hupka, J., Zaleska, A. (2010). Silver-doped TiO₂ prepared by microemulsion method: surface properties, bio- and photoactivity. *Sep. Purif. Technol.*, vol 72, 309-318.

APPENDICES

Gas Pycnometer

CuFe₂O₄



AccuPyc II 1340 V1.05 Unit 1 Serial #: 815 Page 1

Sample: Cu ferrite tsy
 Operator: Reman
 Submitter:
 Bar Code:
 File: C:\1340\DATA\000-740.SMP

Analysis Gas: Helium Analysis Start: 10/31/2014 1:44:09PM
 Reported: 10/31/2014 1:50:31PM Analysis End: 10/31/2014 1:50:31PM
 Sample Mass: 0.4073 g Equilib. Rate: 0.050 psig/min
 Temperature: 26.25 °C Expansion Volume: 12.3230 cm³
 Number of Purges: 3 Cell Volume: 3.8545 cm³

Combined Report
Summary Report

Sample Volume
 Average: 0.1632 cm³
 Standard Deviation: 0.0001 cm³

Sample Density
 Average: 2.4953 g/cm³
 Standard Deviation: 0.0021 g/cm³

Tabular 1

Cycle#	P1 Pressure (psig)	P2 Pressure (psig)	Volume (cm ³)	Density (g/cm ³)	Total Pore Volume (cm ³ /g)
1	19.903	4.588	0.1634	2.4928	0.5988
2	19.941	4.597	0.1631	2.4979	0.5997
3	19.899	4.587	0.1632	2.4953	0.5992
Summary Data			Average	Standard Deviation	
			Volume:	0.1632 cm ³	0.0001 cm ³
			Density:	2.4953 g/cm ³	0.0021 g/cm ³

6202- Total solids concentration is invalid; liquid density is greater-than or equal to solids density.

Tabular 2

Cycle#	P1 Pressure (psig)	P2 Pressure (psig)	Volume (cm ³)	Density (g/cm ³)	Total Pore Volume (cm ³ /g)
1	19.903	4.588	0.1634	2.4928	0.5988
2	19.941	4.597	0.1631	2.4979	0.5997
3	19.899	4.587	0.1632	2.4953	0.5992
Summary Data			Average	Standard Deviation	
			Volume:	0.1632 cm ³	0.0001 cm ³
			Density:	2.4953 g/cm ³	0.0021 g/cm ³

6202- Total solids concentration is invalid; liquid density is greater-than or equal to solids density.

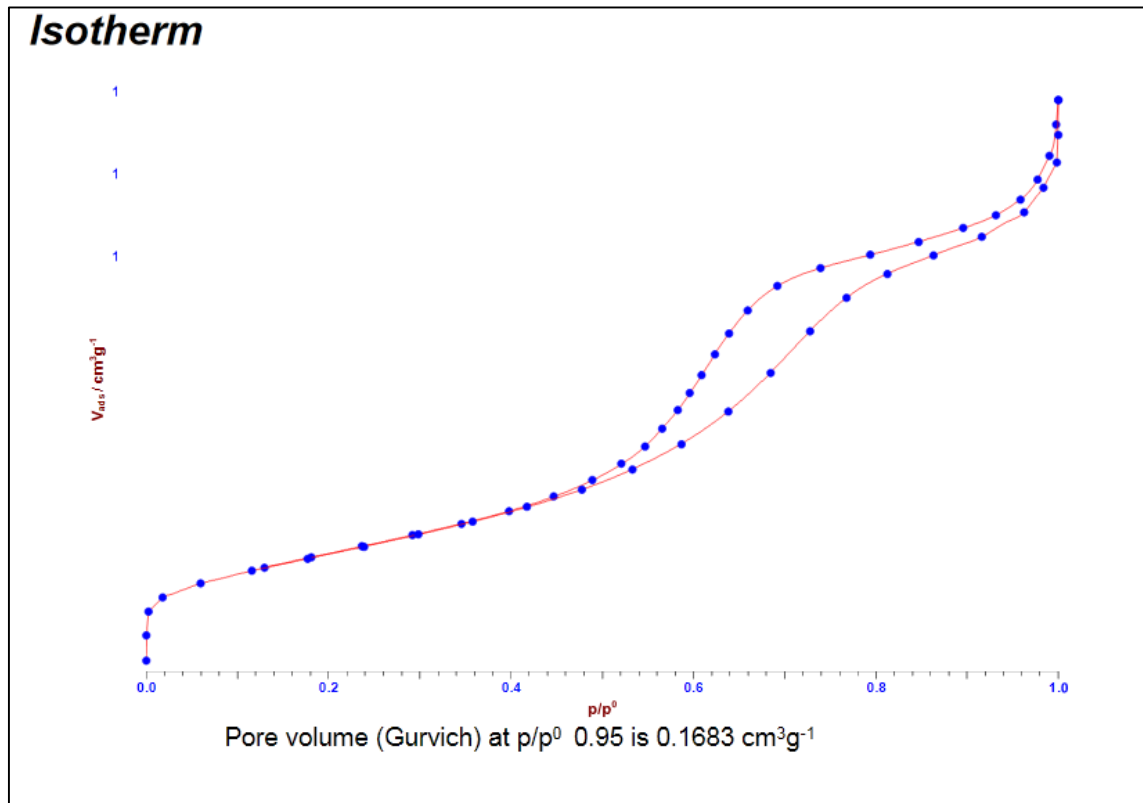
Gas Pycnometer

La-CuFe₂O₄

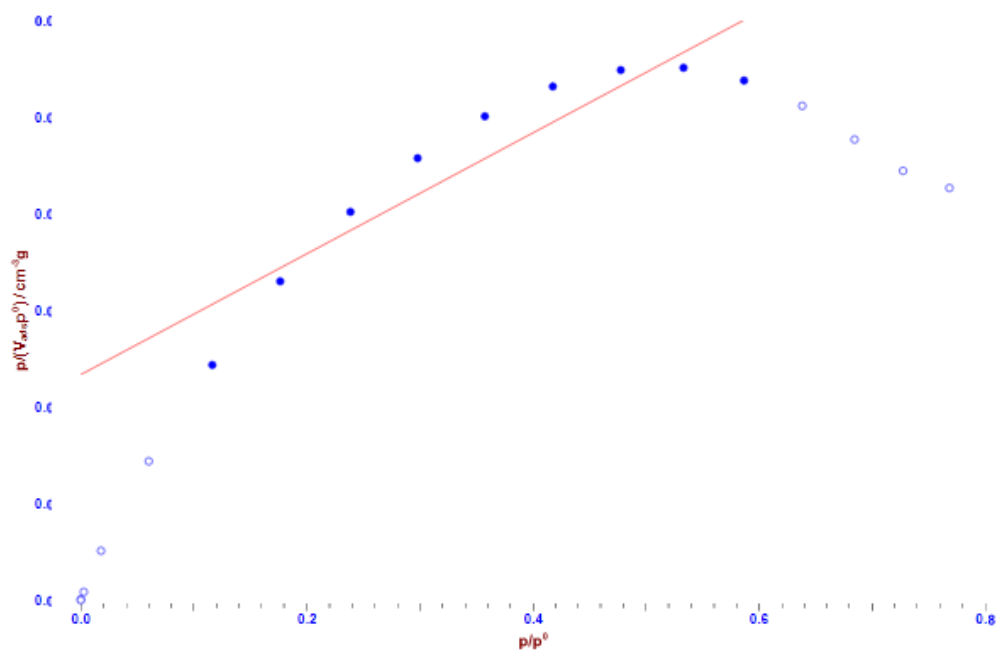
AccuPyc II 1340 V1.05	Unit 1	Serial #: 815	Page 1		
Sample: La/Cu ferrite tsy Operator: Reman Submitter: Bar Code: File: C:\1340\DATA\1000-738.SMP					
Analysis Gas: Helium Reported: 10/31/2014 1:37:46PM Sample Mass: 1.0741 g Temperature: 26.09 °C Number of Purges: 3		Analysis Start: 10/31/2014 1:31:36PM Analysis End: 10/31/2014 1:37:46PM Equilib. Rate: 0.050 psig/min Expansion Volume: 12.3230 cm ³ Cell Volume: 3.8545 cm ³			
Combined Report					
Summary Report					
Sample Volume Average: 0.3092 cm ³ Standard Deviation: 0.0002 cm ³					
Sample Density Average: 3.4734 g/cm ³ Standard Deviation: 0.0018 g/cm ³					
Tabular 1					
Cycle#	P1 Pressure (psig)	P2 Pressure (psig)	Volume (cm ³)	Density (g/cm ³)	Total Pore Volume (cm ³ /g)
1	19.908	4.448	0.3094	3.4714	0.7119
2	20.000	4.468	0.3093	3.4730	0.7121
3	20.019	4.473	0.3090	3.4757	0.7123
Summary Data			Average	Standard Deviation	
			Volume:	0.3092 cm ³	0.0002 cm ³
			Density:	3.4734 g/cm ³	0.0018 g/cm ³
6202- Total solids concentration is invalid; liquid density is greater-than or equal to solids density.					
Tabular 2					
Cycle#	P1 Pressure (psig)	P2 Pressure (psig)	Volume (cm ³)	Density (g/cm ³)	Total Pore Volume (cm ³ /g)
1	19.908	4.448	0.3094	3.4714	0.7119
2	20.000	4.468	0.3093	3.4730	0.7121
3	20.019	4.473	0.3090	3.4757	0.7123
Summary Data			Average	Standard Deviation	
			Volume:	0.3092 cm ³	0.0002 cm ³
			Density:	3.4734 g/cm ³	0.0018 g/cm ³
6202- Total solids concentration is invalid; liquid density is greater-than or equal to solids density.					

BET

CuFe₂O₄



Surface Area (Langmuir)



Linear regression from p/p^0 0.1 to 0.6

Offset: $0.00467752 \pm 0.00074553$

Slope: $0.01251057 \pm 0.00192582$

R: 0.92613526

Monolayer volume $79.932 \text{ cm}^3\text{g}^{-1}$

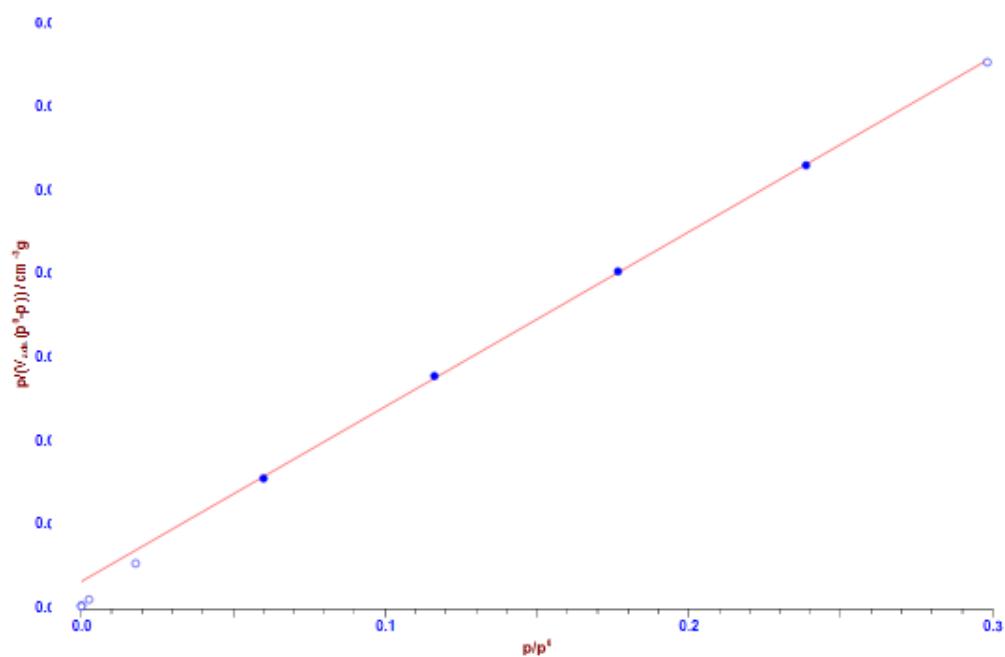
Monolayer amount: $3.5662 \text{ mmol g}^{-1}$

B: 2.6746

Calculation with a molecular area of 16.2 \AA^2

Surface area was: $347.92 \text{ m}^2\text{g}^{-1}$

Surface Area (B.E.T.) 2 Parameters Line



Linear regression from p/p^0 0.05 to 0.25

Offset: $0.0006085 \pm 6.42229\text{E-}5$

Slope: $0.04191188 \pm 0.00039611$

R: 0.99991069

Monolayer volume $23.518 \text{ cm}^3\text{g}^{-1}$

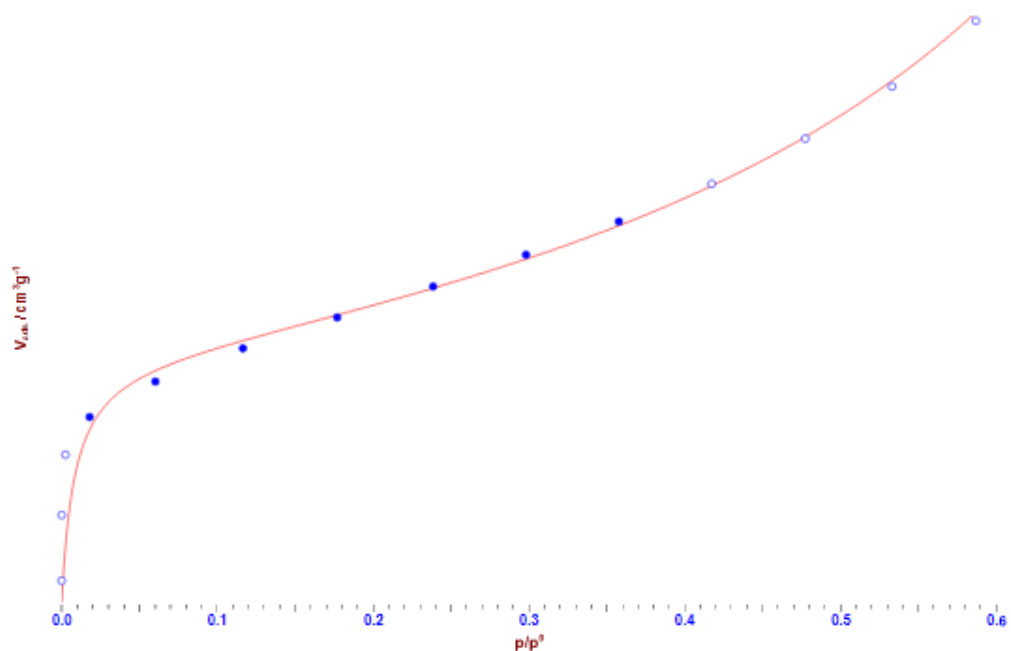
Monolayer amount: $1.0493 \text{ mmol g}^{-1}$

C: 69.877

Calculation with a molecular area of 16.2 \AA^2

Surface area was: $102.37 \text{ m}^2\text{g}^{-1}$

Surface Area (B.E.T.) 3 Parameters Fit



Simplex fit from p/p^0 0.005 to 0.4

r^2 : 0.99044181

Monolayer volume 22.996 $\text{cm}^3 \text{g}^{-1}$

Monolayer amount: 1.026 mmol g^{-1}

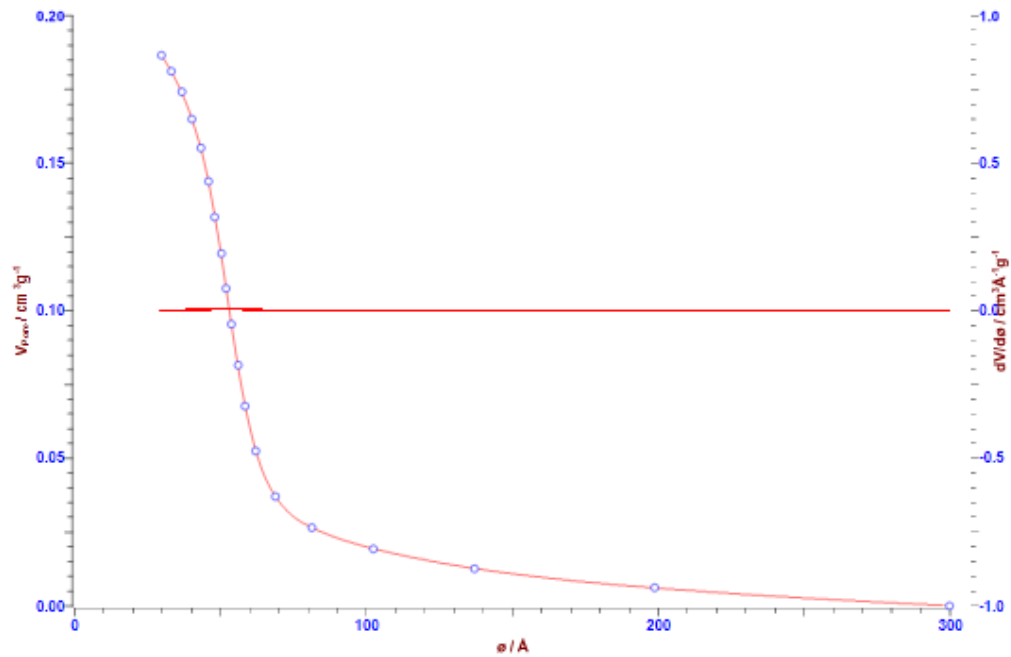
C: 121.62

N: 16.663

Calculation with a molecular area of 16.2 \AA^2

Surface area was: 100.1 $\text{m}^2 \text{g}^{-1}$

Mesopores (B.J.H.)



Calculations used Desorption Branch from p/p^0 0.3 to 0.95

with standard isotherm: Universal (Halsey)

from literature: ASTM Standards Designation: D 4641-87

Calculation with a molecular area of 16.2 \AA^2

molecular weight of 28.01 g/mol

liquid density of 0.8086 g cm^{-3}

and surface tension of $8.85 \text{ Dyne cm}^{-1}$

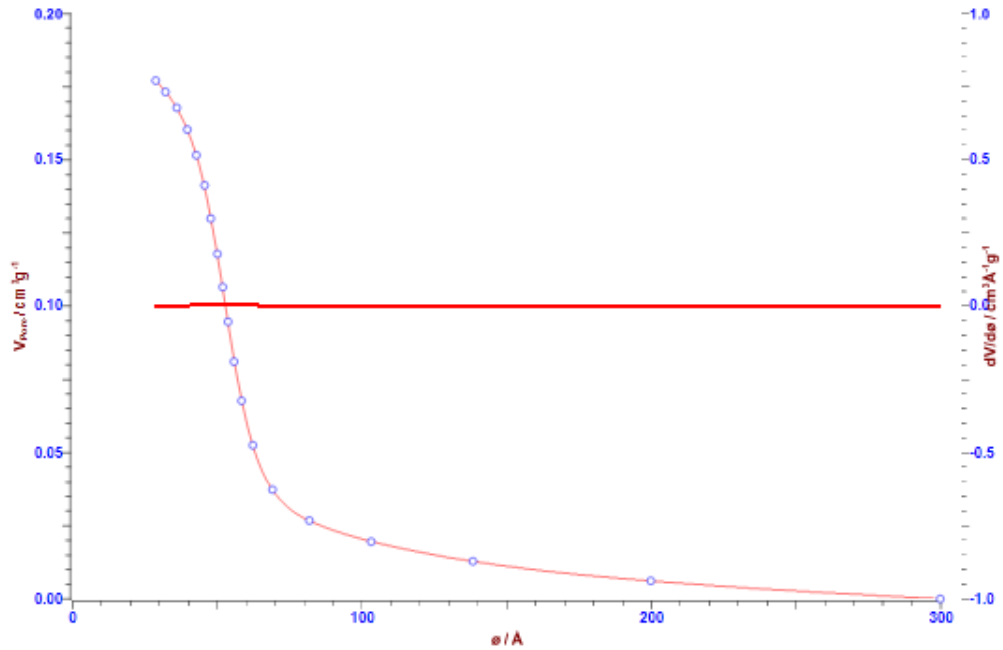
Median pore diameter 54.034 \AA

Maximum pore diameter 52.67 \AA

Cumulative pore volume $0.1866 \text{ cm}^3 \text{g}^{-1}$

Cumulative pore area $136.13 \text{ m}^2 \text{g}^{-1}$

Mesopores (Cranston and Inkley)



Calculations used Desorption Branch from p/p^0 0.3 to 0.95

with standard isotherm: Universal (Harkins, Jura)

from literature: ASTM Standards Designation: D 4641-87

Calculation with a molecular area of 16.2 \AA^2

molecular weight of 28.01 g/mol

liquid density of 0.8086 g cm^{-3}

and surface tension of $8.85 \text{ Dyne cm}^{-1}$

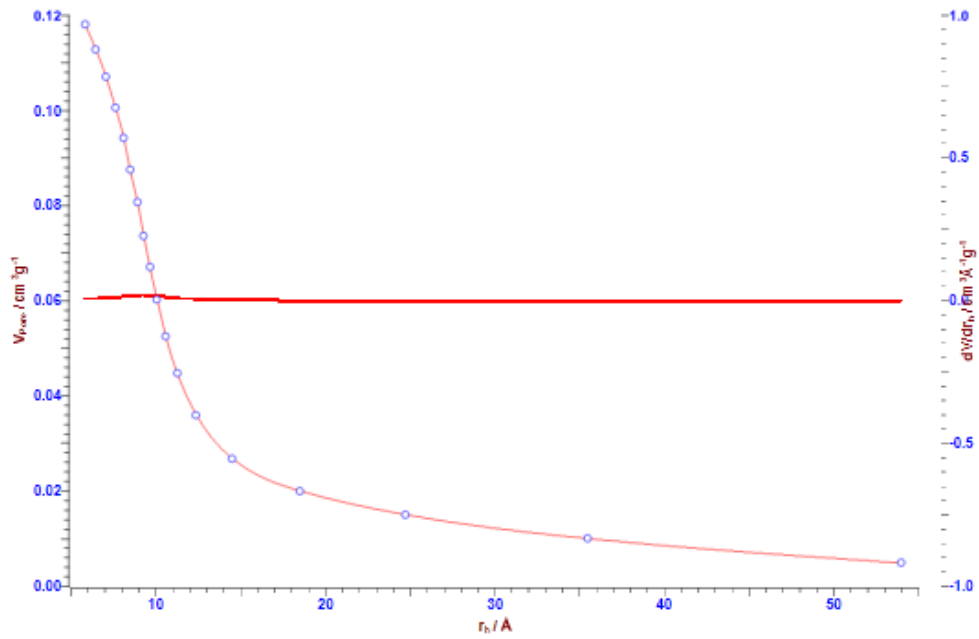
Median pore diameter 54.574 \AA

Maximum pore diameter 52.632 \AA

Cumulative pore volume $0.177 \text{ cm}^3\text{g}^{-1}$

Cumulative pore area $127.11 \text{ m}^2\text{g}^{-1}$

Mesopores (Modelless)



Calculations used Desorption Branch from p/p^0 0.3 to 0.95

with standard isotherm: Universal (Harkins, Jura)

from literature: ASTM Standards Designation: D 4641-87

Calculation with a molecular area of 16.2 \AA^2

molecular weight of 28.01 g/mol

and liquid density of 0.8086 g cm^{-3}

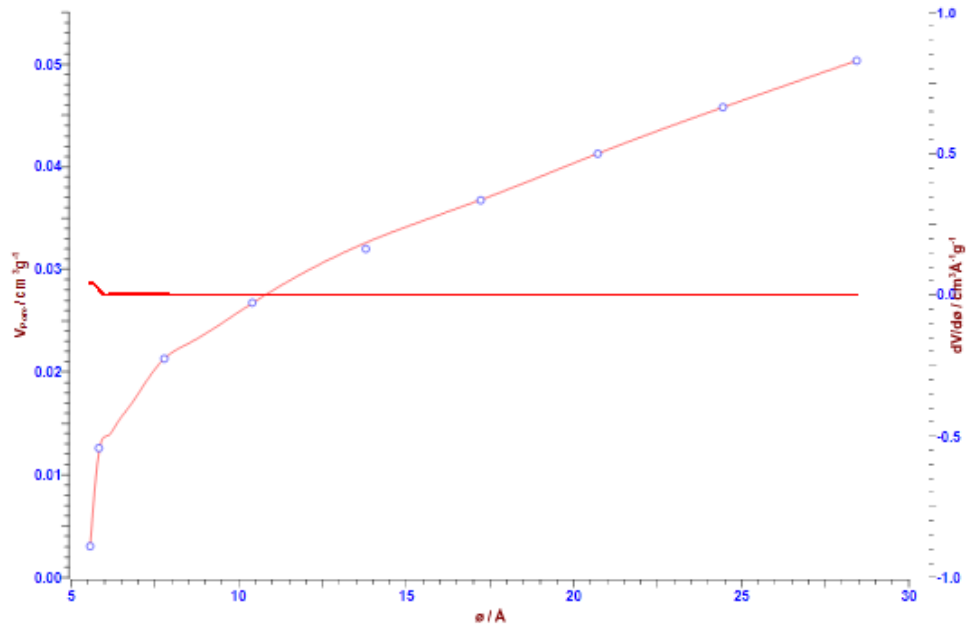
Median hydraulic radius 8.6425 \AA

Maximum hydraulic radius 9.2131 \AA

Cumulative pore volume $0.1699 \text{ cm}^3\text{g}^{-1}$

Cumulative pore area $115.91 \text{ m}^2\text{g}^{-1}$

Micropores (Horvath and Kawazoe)



Calculations from p/p^0 0 to 0.35

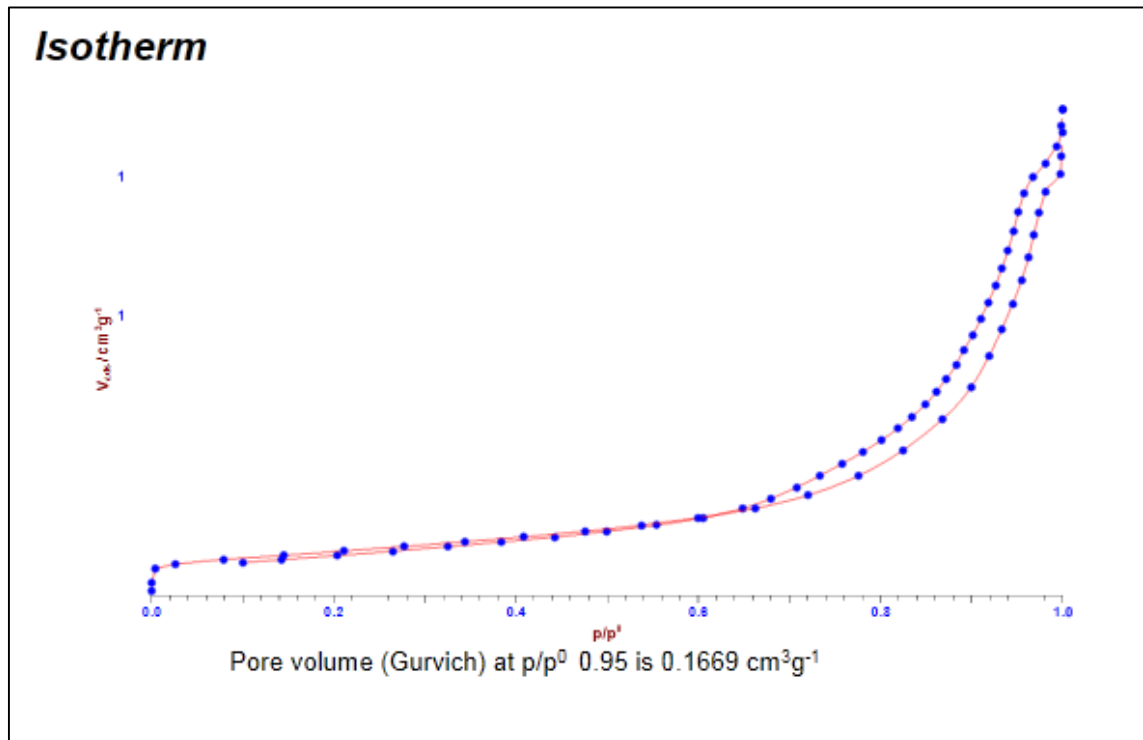
with potential function: Nitrogen on Graphite @77.3 K

from literature: G. Horvath, K. Kawazoe, J. Chem. Eng. Japan, 16, 6(1983), 470-475

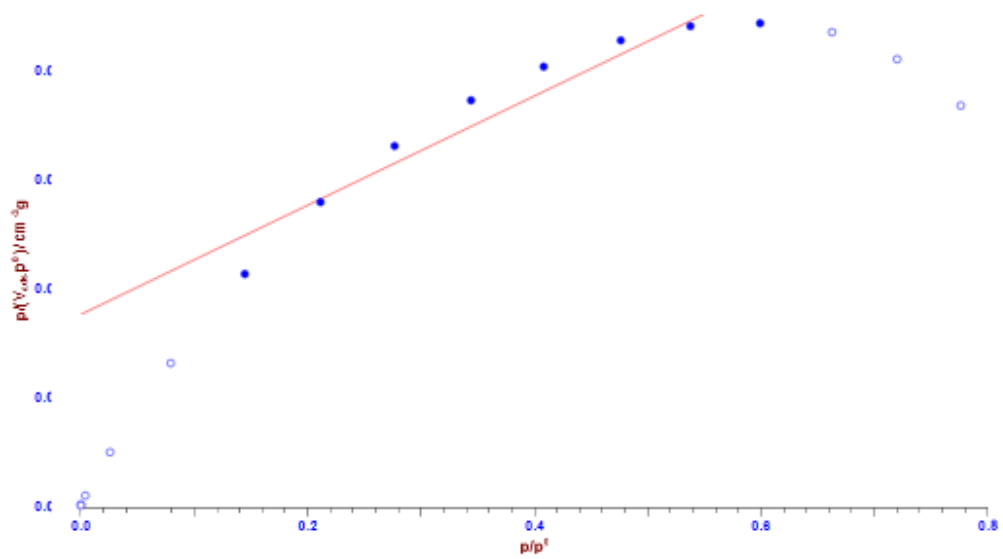
Calculation with a molecular area of 16.2 Å^2
 molecular weight of 28.01 g/mol
 and liquid density of 0.8086 g cm^{-3}
 Median pore diameter 9.4957 Å
 Maximum pore diameter 6.2818 Å
 Cumulative pore volume $0.0503 \text{ cm}^3\text{g}^{-1}$
 Cumulative pore area $100.99 \text{ m}^2\text{g}^{-1}$

BET

La-CuFe₂O₄



Surface Area (Langmuir)

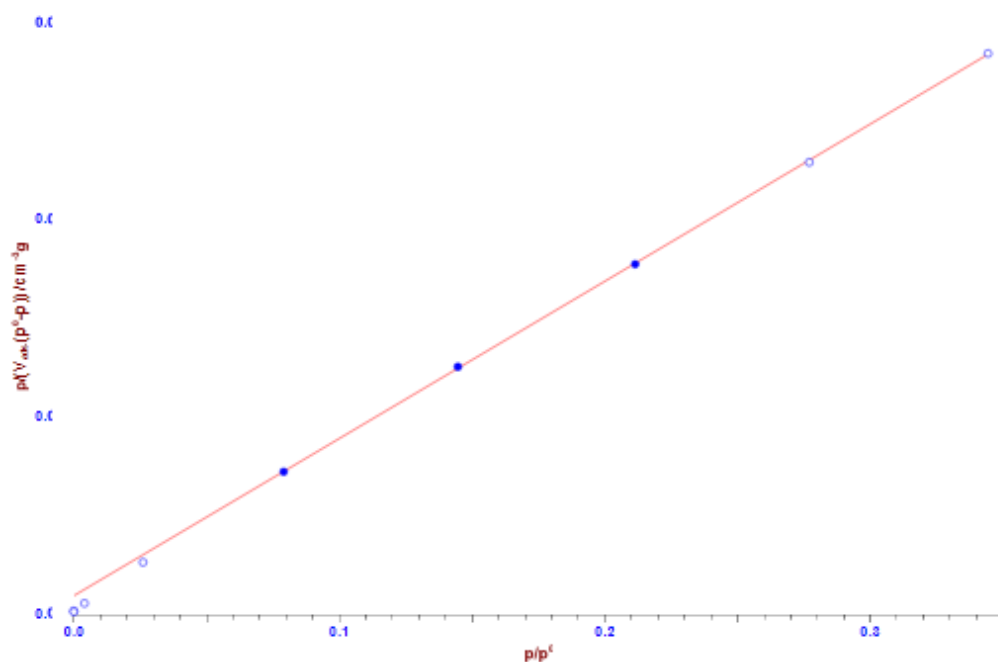


Linear regression from p/p^0 0.1 to 0.6
Offset: $0.00878678 \pm 0.00121539$
Slope: 0.02505986 ± 0.0030115
R: 0.95930243

Monolayer volume $39.904 \text{ cm}^3\text{g}^{-1}$
Monolayer amount: $1.7804 \text{ mmol g}^{-1}$
B: 2.852

Calculation with a molecular area of 16.2 \AA^2
Surface area was: $173.69 \text{ m}^2\text{g}^{-1}$

Surface Area (B.E.T.) 2 Parameters Line



Linear regression from p/p^0 0.05 to 0.25

Offset: $0.00084216 \pm 0.00014143$

Slope: $0.07986133 \pm 0.00091396$

R: 0.99993452

Monolayer volume $12.391 \text{ cm}^3 \text{g}^{-1}$

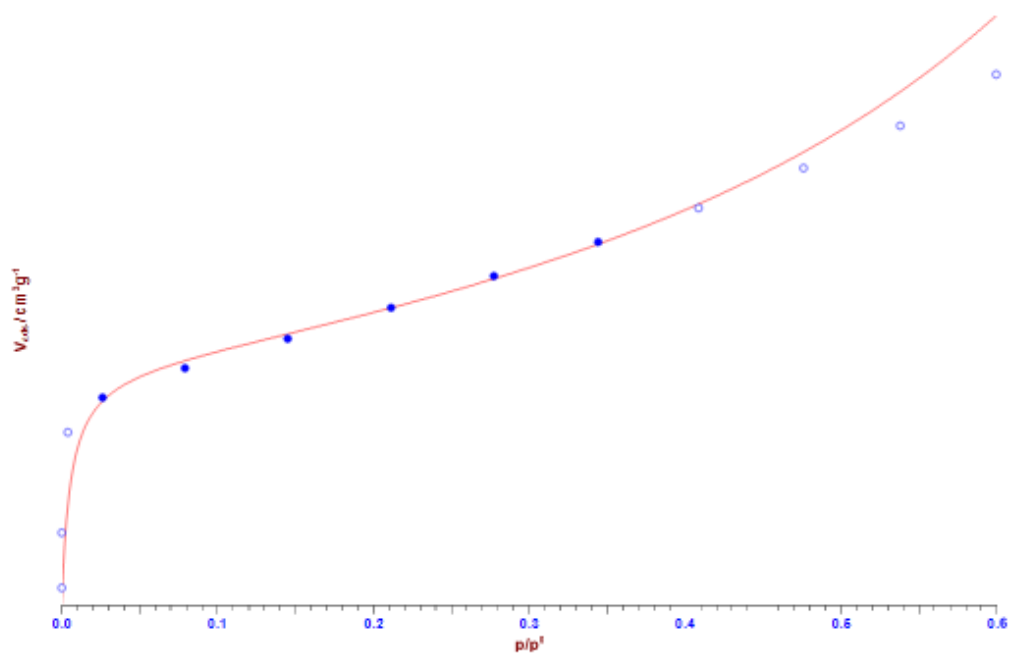
Monolayer amount: $0.5528 \text{ mmol g}^{-1}$

C: 95.829

Calculation with a molecular area of 16.2 \AA^2

Surface area was: $53.934 \text{ m}^2 \text{g}^{-1}$

Surface Area (B.E.T.) 3 Parameters Fit

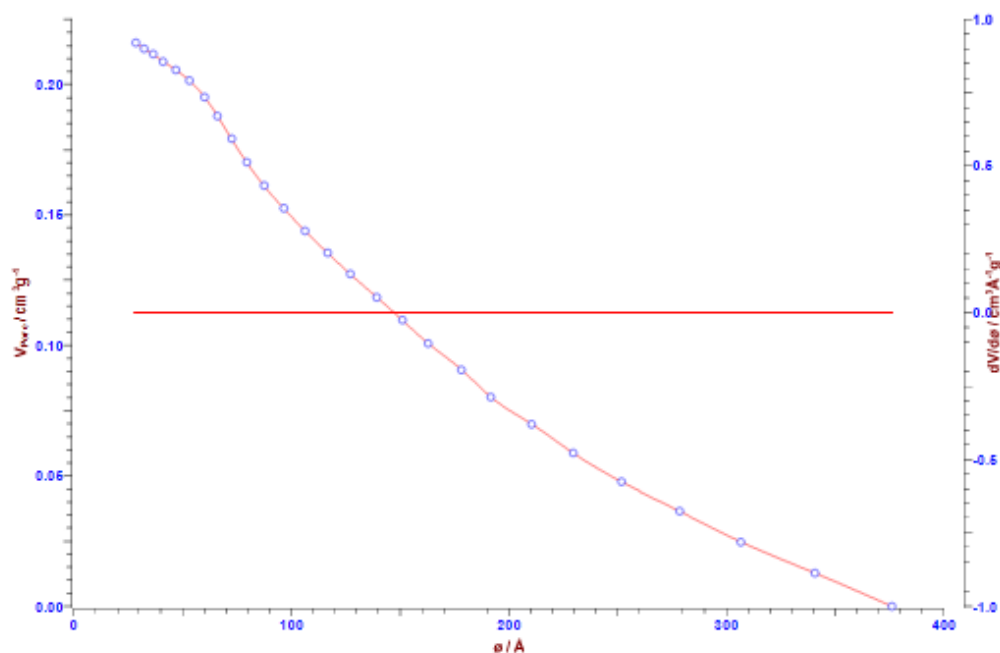


Simplex fit from p/p^0 0.005 to 0.4
 r^2 : 0.99424219

Monolayer volume 12.182 cm^3g^{-1}
Monolayer amount: 0.5435 $mmol g^{-1}$
C: 179.35
N: 12.699

Calculation with a molecular area of 16.2 \AA^2
Surface area was: 53.022 m^2g^{-1}

Mesopores (B.J.H.)



Calculations used Desorption Branch from p/p^0 0.3 to 0.95

with standard isotherm: Universal (Halsey)

from literature: ASTM Standards Designation: D 4641-87

Calculation with a molecular area of 16.2 \AA^2

molecular weight of 28.01 g/mol

liquid density of 0.8086 g cm^{-3}

and surface tension of $8.85 \text{ Dyne cm}^{-1}$

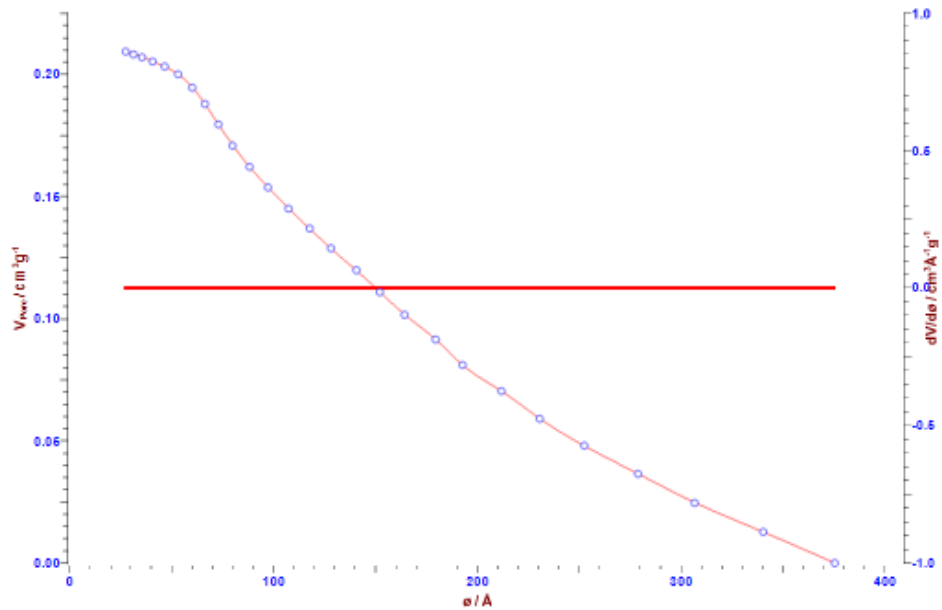
Median pore diameter 153.14 \AA

Maximum pore diameter 69.622 \AA

Cumulative pore volume $0.2159 \text{ cm}^3\text{g}^{-1}$

Cumulative pore area $74.58 \text{ m}^2\text{g}^{-1}$

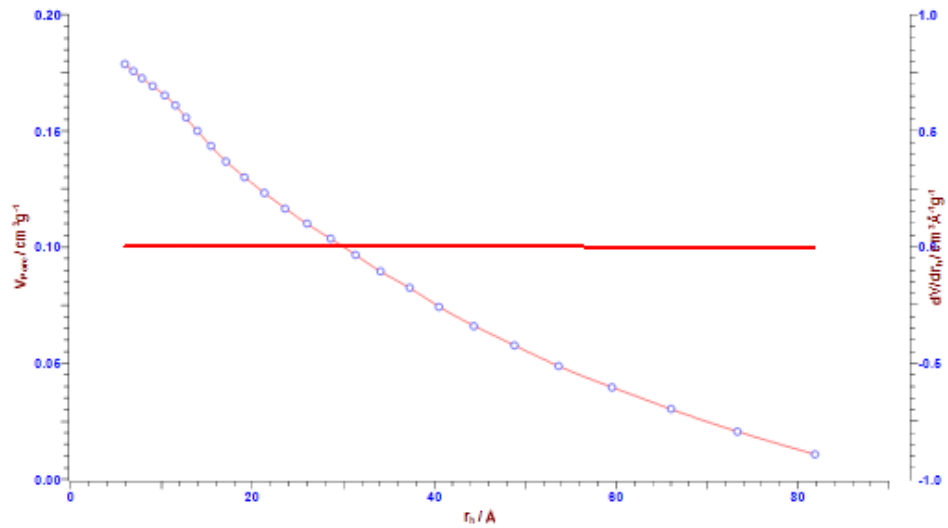
Mesopores (Cranston and Inkley)



Calculations used Desorption Branch from p/p^0 0.3 to 0.95
 with standard isotherm: Universal (Harkins, Jura)
 from literature: ASTM Standards Designation: D 4641-87

Calculation with a molecular area of 16.2 \AA^2
 molecular weight of 28.01 g/mol
 liquid density of 0.8086 g cm^{-3}
 and surface tension of $8.85 \text{ Dyne cm}^{-1}$
 Median pore diameter 160.04 \AA
 Maximum pore diameter 70.383 \AA
 Cumulative pore volume $0.2094 \text{ cm}^3\text{g}^{-1}$
 Cumulative pore area $67.79 \text{ m}^2\text{g}^{-1}$

Mesopores (Modelless)



Calculations used Desorption Branch from p/p^0 0.3 to 0.95

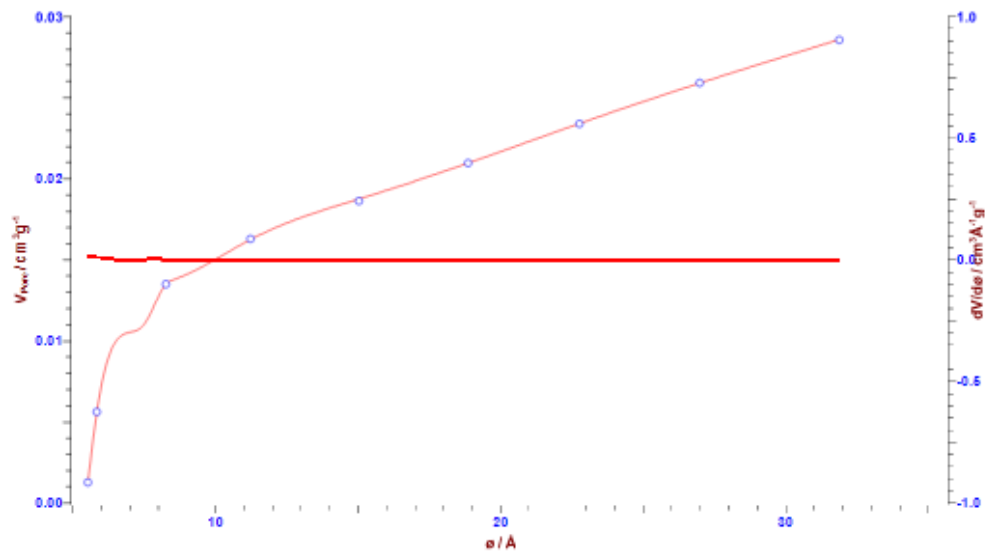
with standard isotherm: Universal (Harkins, Jura)

from literature: ASTM Standards Designation: D 4641-87

Calculation with a molecular area of 16.2 Å^2
 molecular weight of 28.01 g/mol
 and liquid density of 0.8086 g cm^{-3}

Median hydraulic radius 29.793 Å
 Maximum hydraulic radius 12.382 Å
 Cumulative pore volume $0.201 \text{ cm}^3 \text{g}^{-1}$
 Cumulative pore area $78.481 \text{ m}^2 \text{g}^{-1}$

Micropores (Horvath and Kawazoe)



Calculations from p/p^0 0 to 0.35

with potential function: Nitrogen on Graphite @77.3 K

from literature: G. Horvath, K. Kawazoe, J. Chem. Eng. Japan, 16, 6(1983), 470-475

Calculation with a molecular area of 16.2 \AA^2

molecular weight of 28.01 g/mol

and liquid density of 0.8086 g cm^{-3}

Median pore diameter 8.7915 \AA

Maximum pore diameter 7.8454 \AA

Cumulative pore volume $0.0286 \text{ cm}^3\text{g}^{-1}$

Cumulative pore area $54.899 \text{ m}^2\text{g}^{-1}$

XRD

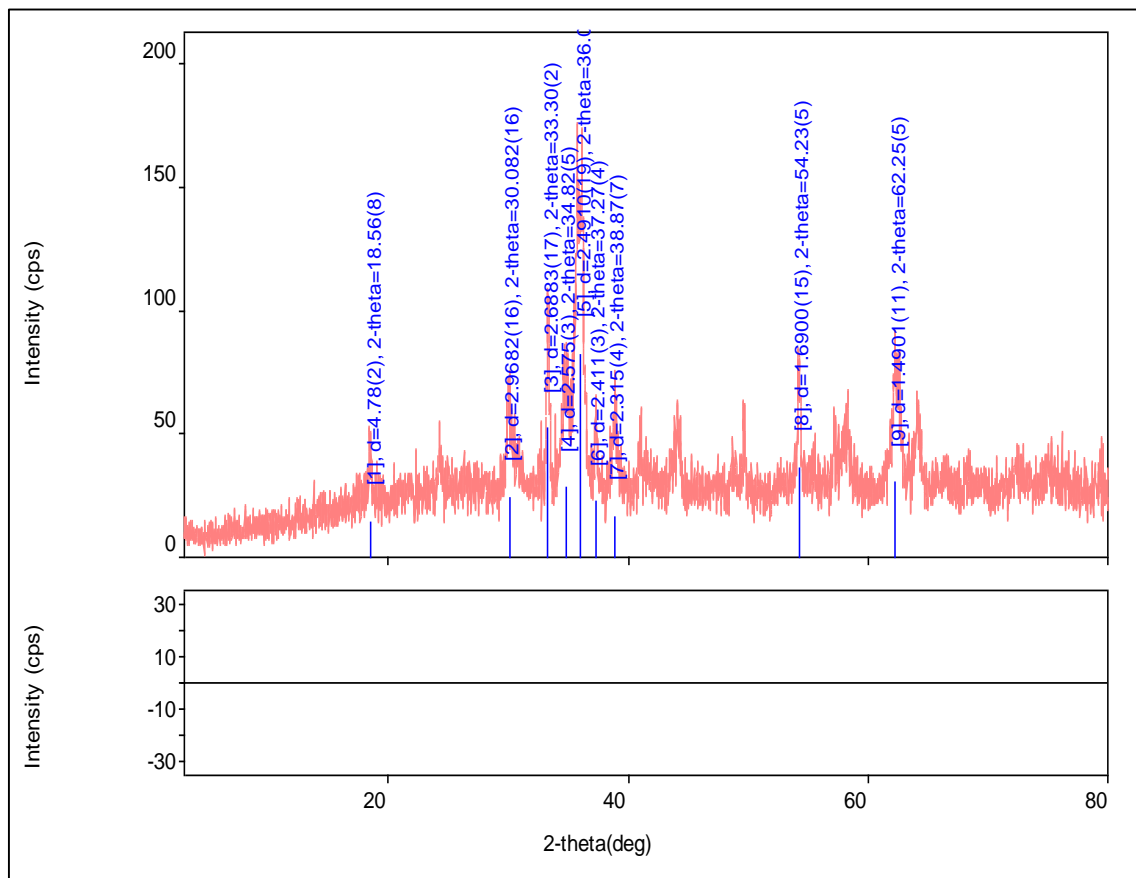
CuFe₂O₄

Analysis Results

General Information

Analysis date	5/8/2014 4:45:43 PM
Sample name	XRD Analysis
File name	2242014.raw
Comment	UMP

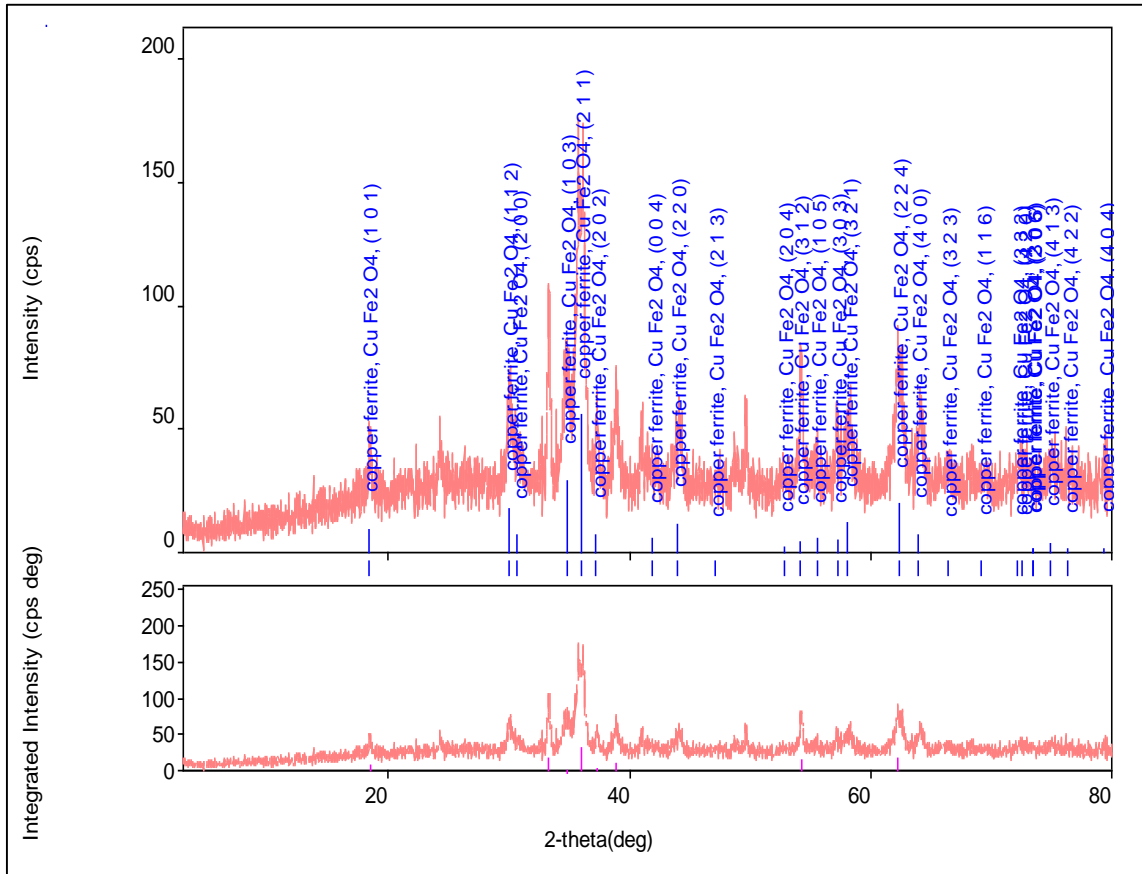
Measurement profile



Qualitative analysis results

Phase name	Formula	Figure of merit	ICDD
copper ferrite	Cu Fe ₂ O ₄	1.124753770650586	340425 (ICDD)

Phase name	Formula	Space group	ICDD
copper ferrite	Cu Fe ₂ O ₄	141 : I41/amd,choice-2	340425 (ICDD)



Peak list

2-theta (deg)	d (ang.)	Height (cps)	Int. I(cps*deg)	FWHM(deg)	Size	Phase name
18.56(8)	4.78(2)	15(4)	6.4(8)	0.27(8)	312(88)	copper ferrite, (1,0,1)
30.082(16)	2.9682(16)	25(5)	17.3(10)	0.51(4)	170(14)	copper ferrite, (1,1,2)
33.30(2)	2.6883(17)	53(7)	13.4(7)	0.226(17)	383(29)	Unknown,
34.82(5)	2.575(3)	29(5)	19.8(16)	0.62(5)	141(11)	copper ferrite, (1,0,3)
36.03(3)	2.4910(19)	83(9)	73(3)	0.80(3)	109(4)	copper ferrite, (2,1,1)
37.27(4)	2.411(3)	23(5)	3.6(6)	0.15(4)	588(148)	copper ferrite, (2,0,2)
38.87(7)	2.315(4)	17(4)	8.3(12)	0.45(6)	195(26)	Unknown,
54.23(5)	1.6900(15)	37(6)	11.4(13)	0.24(6)	396(100)	copper ferrite, (3,1,2)
62.25(5)	1.4901(11)	31(6)	31.3(16)	0.75(5)	129(9)	copper ferrite, (2,2,4)

Lattice constants

Angular correction

No correction
Use External standard parameters
Use internal standard data

Analysis results

File name	a (ang.)	b (ang.)	c (ang.)	alpha (deg)	beta (deg)	gamma (deg)
2242014	5.820370	5.820370	8.617465	90.000000	90.000000	90.000000

Phase name	a (ang.)	b (ang.)	c (ang.)	alpha (deg)	beta (deg)	gamma (deg)
copper ferrite	5.820370	5.820370	8.617465	90.000000	90.000000	90.000000